UNIVERSITY OF PRETORIA

MAGISTER THESIS

Laplace deep-level transient spectroscopy studies of the divacancy in alpha-particle irradiated silicon

---

Author:	*Supervisor:*	*Co-Supervisor:*
H.J.S WEIDEMAN	Prof. W.E. MEYER	Prof. F.D. Auret

A thesis submitted in partial fulfilment of the requirements for the degree of Magister Scientiae

in the

Electronic Materials and Thin Films Research Group
Department of Physics
Faculty of Natural and Agricultural Sciences

February 15, 2024

Declaration of Authorship

I, H.J.S WEIDEMAN, declare that this thesis titled, "Laplace deep-level transient spectroscopy studies of the divacancy in alpha-particle irradiated silicon" and the work presented in it are my own. I confirm that:

- This work was done wholly or mainly while in candidature for a research degree at this University.
- Where any part of this thesis has previously been submitted for a degree or any other qualification at this University or any other institution, this has been clearly stated.
- Where I have consulted the published work of others, this is always clearly attributed.
- Where I have quoted from the work of others, the source is always given. With the exception of such quotations, this thesis is entirely my own work.
- I have acknowledged all main sources of help.
- Where the thesis is based on work done by myself jointly with others, I have made clear exactly what was done by others and what I have contributed myself.

Signed:

Date: 15/02/2024

"If today were the last day of your life, would you want to do what you are about to do today?"

Steve Jobs

"Any man who can drive safely while kissing a pretty girl is simply not giving the kiss the attention it deserves."

Albert Einstein

"There is no substitute for hard work."

Thomas Edison

"Life is tough, but it is tougher if you are stupid."

John Wayne

"Me and my bed are perfect for each other, but my alarm clock keeps trying to break us up."

Anonymous

"If we should not eat at night, why is there a light in the fridge?"

Anonymous

University of Pretoria

Abstract

Faculty of Natural and Agricultural Sciences
Department of Physics

Magister Scientiae

Laplace deep-level transient spectroscopy studies of the divacancy in alpha-particle irradiated silicon

by H.J.S WEIDEMAN

Defects in semiconductors are usually detrimental to the device operation. Particularly in space, the high levels of radiation induce defects that damage electronics in satellites and space craft. However, in some devices defects are crucial to device operation and they are purposely introduced into the semiconductor during manufacture. In both cases it is important to be able to characterise these defects in order to find ways to remove defects that are detrimental and to introduce or keep those defects that are useful.

During this research, the deep-level transient spectroscopy (DLTS) technique was performed on Schottky diodes fabricated on n-type silicon, which were irradiated by alpha particles from an Am^{241} source. In contrast to gamma and electron irradiation, which practically induce only point defects, alpha particles produce some defect clusters as well, especially in the region just before coming to rest. In particular, the two charged states of the divacancy were investigated.

These investigations included the determination of the DLTS signature (the ionisation enthalpy and apparent capture cross-section) of the observed defects. The depth profile and introduction rate of the defects were also determined. This was then compared to previously done research on electron irradiated silicon to determine if any other unknown defects arose from alpha-particle irradiation.

The conventional deep-level transient spectroscopy spectrum showed three discrete peaks at 90 K, 125 K and 225 K, when recorded at a rate window of 80 s^{-1}. By comparison with literature, it was determined that the peak at 90 K was due to both the C_iC_s defect and the VO_i defect, while the peak at 125 K was due to $V_2^{(=/-)}$ defect level and the peak at 225 K was due to the PV defect and the $V_2^{(-/0)}$ defect level.

The annealing profile of both charge states of the peaks due to the divacancy showed annealing in the range 350 K to 400 K, which was not observed in electron-irradiated diodes. We suggest that this is due to defect clusters annealing out, releasing interstitials that combine with the divacancies thereby converting them to highly mobile vacancies. It was also observed that, in the region 550 K to 620 K, where the divacancy anneals, the two peaks annealed by different amounts. This is not the case in electron-irradiated material. We therefore suggest that the $V_2^{(=/-)}$ charge transition level is suppressed by cluster effects.

Acknowledgements

I am grateful to my parents for giving me this opportunity and never stopped supporting me.

I would like to thank my Supervisor Prof. W.E. Meyer and Co-Supervisor Prof. F.D. Auret for their time and support.

Thankful to my friends motivating me, and for being interresred, even though they did not understand.

I would like to thank my colleagues in the Physics Department of the University of Pretoria, help and support.

Thankful to my colleague Mr. Willem Barnard for his time, knowledge and support.

The South African National Research Foundation for their financial assistance during this study.

Finally, I am very grateful to Miss. Amoretha Louw for her undying support and enthusiasm throughout this study.

Contents

Declaration of Authorship 1

Abstract 3

Acknowledgements 4

1 Introduction 13

2 Semiconductor Physics 15
- 2.1 Introduction . . . 15
- 2.2 Crystal Growth Methods . . . 15
  - 2.2.1 Float Zone Growth . . . 15
  - 2.2.2 Czochralski Growth . . . 15
  - 2.2.3 Epitaxial Growth . . . 16
- 2.3 Crystal Structure . . . 16
- 2.4 Band Structure . . . 17
- 2.5 Carrier Concentration at Thermal Equilibrium . . . 20
  - 2.5.1 Intrinsic Case . . . 21
  - 2.5.2 Extrinsic Case . . . 22

3 Metal–Semiconductor Junctions 26
- 3.1 Introduction . . . 26
- 3.2 Ideal Schottky Barrier . . . 26
  - 3.2.1 Forward and Reverse Bias . . . 28
  - 3.2.2 Depletion Region . . . 29
- 3.3 Current Transport Mechanisms . . . 30
- 3.4 Ohmic Contacts . . . 32

4 Defects in Semiconductors 34
- 4.1 Introduction . . . 34
- 4.2 Defect Generation . . . 34
- 4.3 Classification of Defects . . . 36
  - 4.3.1 Clusters . . . 36
  - 4.3.2 Point Defects . . . 36
- 4.4 Electrical Properties of Point Defects . . . 37
  - 4.4.1 Occupation of Traps at Thermal Equilibrium . . . 37
  - 4.4.2 Energy and Gibbs Free Energy . . . 38
  - 4.4.3 Carrier Recombination Processes . . . 39
  - 4.4.4 Defect Occupation with Time . . . 41
  - 4.4.5 Defect Occupation under Bias . . . 41
- 4.5 Defect Introduction . . . 42
  - 4.5.1 Zeroth-Order . . . 42
  - 4.5.2 First-Order . . . 43

4.6 Defect Annealing . . . 44
4.6.1 Annealing Mechanisms . . . 44
4.6.2 Reaction Rate . . . 45
4.7 Electric Field Dependence . . . 46
4.7.1 Poole-Frenkel Effect . . . 46
4.7.2 Phonon-Assisted Tunnelling . . . 47

5 Characterisation Techniques 49
5.1 Introduction . . . 49
5.2 Current-Voltage Characterisation . . . 49
5.3 Capacitance-Voltage Characterisation . . . 50
5.4 Deep-level Transient Spectroscopy . . . 50
5.4.1 Capacitance Transient . . . 51
5.4.2 Conventional DLTS (C-DLTS) . . . 53
5.4.3 Laplace DLTS (L-DLTS) . . . 54
5.5 Emission Activation Energy . . . 55
5.6 Defect Depth Profiling . . . 57

6 Experimental Techniques 60
6.1 Introduction . . . 60
6.2 Sample Preparation . . . 60
6.2.1 Cleaning Procedure . . . 60
6.2.2 Contact Formation . . . 61
6.3 Sample Irradiation . . . 62
6.4 Experimental Setup . . . 63
6.4.1 Current-Voltage and Capacitance-Voltage Setup . . . 63
6.4.2 Deep-Level Transient Spectroscopy Setup . . . 64
6.4.3 Annealing Setup . . . 66

7 Results and Discussion 67
7.1 Introduction . . . 67
7.2 Annealing Profiles . . . 70
7.3 Activation Energy and Apparent Capture Cross-Section . . . 74
7.4 Introduction Profile . . . 76
7.5 Depth Profile . . . 77
7.6 Electric Field Effect . . . 79

8 Conclusions 81

List of Figures

2.1 Illustrates the cubic unit cells: (a) simple-cubic, (b) body-centered cubic, and (c) face-centered cubic. 17
2.2 Illustrates the diamond or zincblende unit cell. All atoms are the same for diamond unit cell, and different for each sublattice in the zincblende unit cell. 17
2.3 Energy band diagram for silicon and germanium. [4] 19
2.4 Energy-band diagram showing when: (a) donor impurity, and (b) acceptor impurity atoms have been added. 22
2.5 Electron density as function of temperature for n-type silicon. [10] . . . 25

3.1 The formation of a metal and n-type semiconductor Schottky barrier: (a) metal and semiconductor in their isolated states, and (b) in intimate contact. [14] 27
3.2 The formation of a metal and p-type semiconductor Schottky barrier: (a) metal and semiconductor in their isolated states, and (b) in intimate contact. [14] 28
3.3 Current transport mechanisms under forward bias: (1) thermionic emission, (2) quantum-mechanical tunnelling, (3) generation and recombination of carriers, and (4) injection of minority carriers. [4] 31
3.4 The formation of a metal and n-type semiconductor Ohmic contact: (a) low barrier height, and (b) high doping concentration. [4] 33

4.1 Illustrates some of the point defects: (a) vacancy, (b) interstitial, (c) impurity substitution, (d) impurity interstitial and (e) Frenkel pair. [22] 35
4.2 Simulation of the spatial distribution of vacancies formed after irradiation with neutrons. [24] 35
4.3 Observed point defects in the band gap of silicon. [27] 36
4.4 Single-level recombination processes for indirect band gap semiconductors: (a) electron capture, (b) electron emission, (c) hole capture, and (d) hole emission. With the top before recombination and the bottom after recombination. [30] 39
4.5 Simulation showing the concentration of defects following the zeroth-order and the first-order introduction rates, with the expected concentration of both defects combined. 43
4.6 Illustrates the mechanism and corresponding activation energy: (a) defect migration, (b) complex formation, and (c) complex dissociation. [32] 44
4.7 Illustrates a Coulombic potential well, with (a) no external electric field and (b) with an external electric field applied. [17] 46

5.1 DLTS principle of operation, and transient formation. 52

5.2 Illustrates how the conventional DLTS spectra are formed from the capacitance transient changes as a function of temperature. [43] 54
5.3 DLTS signals for different rate window conditions. 56
5.4 Arrhenius plot obtained from DLTS signal maxima. 56
5.5 The energy band diagram and charge density as a function of depth for Schottky diode. The solid line corresponding to the charge distribution under a quiescent reverse bias and the dashed lines is the charge distribution right after the filling pulse which relaxes back to solid line. [47] 57
5.6 DLTS signals obtained during depth profiling. On the left we have the filling pulse applied to the Schottky diode, with the bottom being the smallest filling pulse and the top the largest filling pulse. On the left is the corresponding signals obtained through DLTS and L-DLTS measurments. DLTS 59

6.1 Schematic diagram of the resistive thermal evaporation system used to deposit the Ohmic and Schottky contacts. 61
6.2 Schematic diagram showing a sample with both the Schottky and ohmic contacts deposited using resistive thermal evaporation, with (a) the side view and (b) the top view of the sample. 62
6.3 Shows the decay process of Americium-241 with the respective energies and percentage. [49] 62
6.4 Shows the TRIM simulation of 100 nm gold-antimony on 200μm of silicon irradiated with alpha particles with 5.4 MeV of energy. 63
6.5 Schematic diagram showing the system setup used for the current-voltage and capacitance-voltage measurements. 64
6.6 Schematic diagram showing the system setup used for deep-level transient spectroscopy. [51] 65

7.1 Conventional deep-level transient spectroscopy spectrum of an n-type silicon Schottky diode after room temperature irradiation with alpha particles. These measurements were recorded at a quiescent reverse bias of V_R = -2 V, with a filling pulse of V_p = 0 V, pulse width of 1 ms and a rate window of 80 s^{-1}. 68
7.2 Conventional deep-level transient spectroscopy spectra of the alpha particle irradiated sample after isochronal annealing consisting of 10 K steps for 15 min each. These measurements were recorded at a quiescent reverse bias of V_R = -2 V, with a filling pulse of V_p = 0 V, pulse width of 1 ms and a rate window of 80 s^{-1}. 70
7.3 Isochronal annealing of the peak at 125 K associated with the double negative divacancy directly after alpha particle irradiation measured at a depth of 1 μm. Annealing was done at 10 K steps for 15 min each. The line plots is drawn using a program to show the three distinct annealing processes. 71
7.4 Isochronal annealing of the single negative divacancy directly after alpha particle irradiation measured at 225 K at a depth of 1 μm. Annealing was done at 10 K steps for 15 min each. The line plots is drawn using a program to show the three distinct annealing processes. 72
7.5 Arrhenius plot obtained for the single negative divacancy (red) and single negative phosphorous vacancy after annealing and the double negative divacancy before (black) and after (green) annealing. 74

7.6 Defect concentration of the double negative divacancy as function of time directly after alpha particle irradiation (black) and after annealing (red) at 530 K for 60 min. 76
7.7 Depth profile of the double negative divacancy after isochronal annealing at set temperatures. 77
7.8 Depth profile of the single negative divacancy after isochronal annealing at set temperatures. 78
7.9 Electric field dependence of the double negative divacancy after annealing. With the left hand side Poole-Frenkel effect and the right hand side phonon-assisted tunnelling. 79
7.10 Electric field dependence of the single negative divacancy after annealing. With the left hand side Poole-Frenkel effect and the right hand side phonon-assisted tunnelling. 80

List of Tables

2.1 Band gap energy for some semiconductors at absolute zero and at room temperature. 20
2.2 Electron and hole mobility for some semiconductors at room temperature. 20

7.1 Comparing the literature values of the radiation-induced defects in silicon after particle irradiation at room temperature with the experimental values obtained during this study. 69
7.2 Comparing the literature values of the radiation-induced defects in silicon after particle irradiation at room temperature with the experimental values obtained during this study. 75

List of Abbreviations

VPE	**V**apor **P**hase **E**pitaxy
LPE	**L**iquid **P**hase **E**pitaxy
SPE	**S**olid **P**hase **E**pitaxy
MBE	**M**olecular-**B**eam **E**pitaxy
RF	**R**adio-**F**requency
SC	**S**imple **C**ubic
BCC	**B**ody-**C**entered **C**ubic
FCC	**F**ace-**C**entered **C**ubic
SBD	**S**chottky **B**arrier **D**iode
DLTS	**D**eep-**L**evel **T**ransient **S**pectroscopy
L-DLTS	**L**aplace **D**eep-**L**evel **T**ransient **S**pectroscopy
MOS	**M**etal-**O**xide-**S**emiconductor
CMOS	**C**omplementary **M**etal-**O**xide-**S**emiconductor
MOSFET	**M**etal-**O**xide-**S**emiconductor **F**ield-**E**ffect **T**ransistor
RTE	**R**esistive **T**hermal **E**vaporation
IV	**C**urrent-**V**oltage
CV	**C**apacitance-**V**oltage
SNR	**S**ignal-to-**N**oise **R**atio

Physical Constants

Avogadro Constant	$N_A = 6.022\,04 \times 10^{23}\,\mathrm{mol^{-1}}$
Bohr Radius	$a_B = 0.529\,17\,\text{Å}$
Boltzmann Constant	$k_B = 1.380\,66 \times 10^{-23}\,\mathrm{J\,K^{-1}}$
Electron Rest Mass	$m_0 = 0.910\,95 \times 10^{-30}\,\mathrm{kg}$
Proton Rest Mass	$M_p = 1.672\,64 \times 10^{-27}\,\mathrm{kg}$
Electron-Volt	$eV = 1.602\,18 \times 10^{-19}\,\mathrm{J}$
Elementary Charge	$q = 1.602\,18 \times 10^{-19}\,\mathrm{C}$
Gas Constant	$R = 8.314\,\mathrm{J\,mol^{-1}\,K^{-1}}$
Permeability in Vacuum	$\mu_0 = 1.256\,63 \times 10^{-6}\,\mathrm{H\,m^{-1}}$
Permittivity in Vacuum	$\epsilon_0 = 8.854\,18 \times 10^{-12}\,\mathrm{F\,m^{-1}}$
Planck Constant	$h = 6.626\,17 \times 10^{-34}\,\mathrm{J\,s}$
Reduced Planck Constant	$\hbar = 1.054\,58 \times 10^{-34}\,\mathrm{J\,s}$
Speed of Light in Vacuum	$c = 2.997\,92 \times 10^{8}\,\mathrm{m\,s^{-1}}$

Chapter 1

Introduction

Silicon is one of the most abundant elements on earth and occurs in nature as silica (SiO_2) and never in its pure elemental form. In 1787, Lavoisier suggested that silica was an oxide of some unknown element. Since then a lot of research was done to break silica into its elemental form. By 1854, a breakthrough was made when silicon was reproducibly obtained by Saint-Claire Deville, who crystallised it from electrolysis of mixed chlorides. [1] After this, silicon was used in different fields, with its semiconducting properties discovered in 1874 by Karl Ferdinand Braun, but it was not until 1954 that the first commercial transistor was made available to the public.

Radiation-induced defects in silicon have been studied for many years now, firstly to determine the structure and properties of the defects introduced and secondly to determine the effects of these radiation-induced defects on the electrical properties of electronic devices. In early studies of radiation-induced defects in silicon electronic devices the focus was on the unwanted effects of defects. However, it has become clear that radiation-induced defects can, in some cases, be beneficial to device properties, thus opening a new field of research and development. This new-found field led to new process techniques for fabrication, to incorporate these radiation-induced effects. [2]

In this study phosphorous doped silicon wafers were cut into workable pieces and metal contacts was placed onto them in order to do the electrical measurements. These workable pieces were now referred to as the samples will be irradiated with alpha-particles. Many of the common defects found in silicon will be observed, but we will be focusing mainly on the two charged states of the divacancy, and show through the help of deep-level transient spectroscopy that the observed peaks are not only the divacancy and clusters-related defects, but also consists of a third unknown defect which is not cluster related.

Many of the electrical and physical properties of silicon will be discussed. Below is a short summary of the topics that will be covered in each of the following chapters:

- Chapter 2: This chapter starts out by describing the different growth methods used to grow single crystal structures. Hereafter, the crystal structure and band structure of silicon will be discussed. The carrier concentration for the intrinsic and extrinsic cases will be derived.

- Chapter 3: Metal-semiconductor contacts are crucial in semiconductor physics and play an important role in semiconductor characterisation. Thus this chapter is devoted to discussing the formation of the ideal Schottky barrier and

Ohmic contact. Hereafter, the formation of the depletion region is discussed in more detail and the mechanisms according to which current may be transported across the Schottky barrier will be discussed briefly.

- Chapter 4: In this chapter different radiation-induced defects in crystalline silicon and the mechanism and rate of introduction as well as the annealing mechanisms will be considered briefly. The electrical properties of these defects states under non-equilibrium and equilibrium conditions will be discussed in more detail.

- Chapter 5: Deep-level transient spectroscopy is a powerful technique based on the observation of thermal emission of charge carriers from traps in the forbidden band gap. This chapter will be devoted to describe the deep-level transient spectroscopy technique in detail. Afterwards, specific types of measurement techniques using deep-level transient spectroscopy will be discussed.

- Chapter 6: This chapter describes the preparation of the samples used in this study. The rest of the chapter will be devoted to a detailed description of the instrumentation and how it was set up.

- Chapter 7: All the results obtained from deep-level transient spectroscopy and other characterisation techniques are presented and discussed in this chapter.

- Chapter 8: Final comments, conclusions and future research are discussed in this chapter.

Chapter 2

Semiconductor Physics

2.1 Introduction

Semiconductor materials can simplistically be defined as materials having conductivities between those of metals and insulators. Semiconductors can be classified into two groups, elemental semiconductors which are found in group IV of the periodic table, and compound semiconductors, which are composed of two or more elements. It is important to understand the physics behind semiconductor materials, as it plays a crucial role in understanding semiconductor devices. This chapter gives a short overview, for a more detailed explanation the reader is referred to Neaman [3] or Sze [4].

In Section 2.2 we will start out describing the different methods by which semiconductor crystals are fabricated. In Section 2.3 the crystal structures are defined, while Section 2.4 describes how the band structure can be determined by solving the Schrodinger equation for a large number of electrons interacting with atoms in a crystalline solid. Finally, in Section 2.5 the number of charge carriers for intrinsic and extrinsic semiconductors are calculated at thermal equilibrium.

2.2 Crystal Growth Methods

There are three common methods used to grow single crystal silicon. Each of these processes, which will be discussed below, introduce different kinds and concentrations of impurities.

2.2.1 Float Zone Growth

During this process a rotating poly-crystalline silicon rod is passed through a radio-frequency heating coil, partly melting the silicon. Another rotating rod containing the seed crystal is then brought into contact with the molten silicon at one end. The heating coil is then moved along the rod, which moves the molten section along the rod. As the silicon cools, it solidifies into a single crystal. This is all done in an evacuated chamber or under an inert gas. Some impurities, such as carbon and oxygen, are still present at very low concentrations.

2.2.2 Czochralski Growth

In this process poly-crystalline silicon is melted in a rotating quartz crucible, with a radio-frequency heating coil. A seed crystal attached to a rotating rod is placed on the surface of the molten silicon, and then gradually lifted upwards. As the rod

is pulled out of the molten silicon, a single crystal grows from the seed crystal and is pulled from the melt. If required, dopants may be added to the molten silicon. Growth is performed under an inert gas. During this process oxygen are introduced as impurities.

2.2.3 Epitaxial Growth

Epitaxy refers to the deposition of a crystalline layer on a crystalline substrate. Thus epitaxial layers are grown as thin films on the crystal substrate. The orientation of the surface atoms of the substrate determines the orientation of the thin film. Each epitaxial layer can be doped by adding dopants (elemental impurities) to the source gas during the growth process. This also allows for the possibility of adding different kinds of impurities to different epitaxial layers.

There are many different methods for epitaxial growth including vapour phase, liquid phase, solid phase and molecular-beam epitaxy. Vapour phase epitaxy is usually used for growing silicon, whereas molecular-beam and liquid-phase epitaxy are mainly used for compound semiconductors.

2.3 Crystal Structure

A crystal structure is a periodic arrangement of atoms, each crystal structure consists of repeated unit cells. A unit cell is a group or arrangement of atoms that, when repeated describes a crystal structure. Every crystal structure can be described by three basis vectors, in such a way that the crystal structure remains invariant under translation by any multiples of these basis vectors. [5] In other words the lattice sites can be defined as:

$$\mathbf{R} = m\mathbf{a} + n\mathbf{b} + p\mathbf{c} \tag{2.1}$$

For each set of basis vectors of the direct lattice, with m, n and p any integer values, there exists a set of reciprocal lattice basis vectors defined as:

$$\mathbf{a}^* = 2\pi\frac{\mathbf{b}\times\mathbf{c}}{\mathbf{a}\cdot\mathbf{b}\times\mathbf{c}} \qquad \mathbf{b}^* = 2\pi\frac{\mathbf{c}\times\mathbf{a}}{\mathbf{a}\cdot\mathbf{b}\times\mathbf{c}} \qquad \mathbf{c}^* = 2\pi\frac{\mathbf{a}\times\mathbf{b}}{\mathbf{a}\cdot\mathbf{b}\times\mathbf{c}} \tag{2.2}$$

The reciprocal lattice can be defined in the same manner as the direct lattice:

$$\mathbf{G} = h\mathbf{a}^* + k\mathbf{b}^* + l\mathbf{c}^* \tag{2.3}$$

Using the above-mentioned equations it can easily be shown that each vector in the reciprocal lattice is normal to a set of planes inside the direct lattice, it can also be shown that the volume of a unit cell of the reciprocal lattice is inversely proportional to the volume of a unit cell of the direct lattice.

Figure 2.1 illustrates three of the most basic but important cubic unit cells, these unit cells forms the basis for more complex crystal structures. The simple-cubic unit cell has one atom on each vertex, the body-centered cubic has an extra atom in the middle of the cube, and the face-centered cubic has an extra atom on each face of the cube.

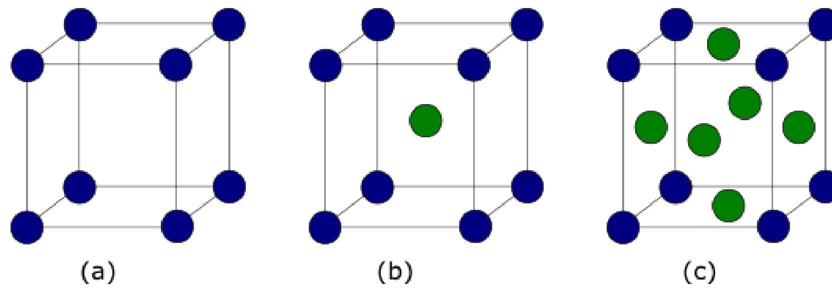

FIGURE 2.1: Illustrates the cubic unit cells: (a) simple-cubic, (b) body-centered cubic, and (c) face-centered cubic.

The diamond and zincblende lattices are formed by two interpenetrating face-centered cubic lattices offset by a quarter body diagonal, as shown in Figure 2.2. Many of the elemental semiconductors, such as silicon, or germanium crystallise according to the diamond lattice structure. Whereas many of the compound semiconductors, such as gallium arsenide or gallium nitride, crystallise into the zincblende lattice structure. In the diamond lattice all of the atoms are the same, and in the zincblende lattice each sublattice describes the positions of one of the two elements forming the compound semiconductor. In both cases each of the atoms are bonded covalently to four nearest neighbour atoms in a tetrahedral arrangement.

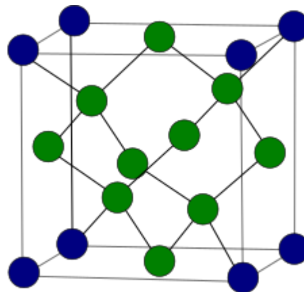

FIGURE 2.2: Illustrates the diamond or zincblende unit cell. All atoms are the same for diamond unit cell, and different for each sublattice in the zincblende unit cell.

From Figure 2.1 and 2.2 it can be seen that the arrangement of atoms in a plane through the crystal lattice in not the same for all planes. This in turn causes distinct properties in different orientations of the crystal surface. Thus it is necessary to have a way to describe these different planes within the crystal structure. This is done by using Miller indices, which are determined by finding the intercepts of the plane with the basis axes in terms of the three basis vectors, and then taking the reciprocal of these values, and finally reducing them to smallest integer values having the same ratio. Some important lattice planes for cubic unit cells are the $\{100\}$, $\{110\}$ and the $\{111\}$ planes. [4]

2.4 Band Structure

By solving the Schrödinger equation we can obtain the energy-momentum relationship of electrons in the crystalline solid. This relationship is commonly referred to

as the band structure of the solid. Bloch's theorem states that if a potential $V(\mathbf{r})$ is periodic with the lattice periodicity, the solutions to the Schrödinger equation:

$$[-\frac{\hbar^2}{2m}\nabla^2 + V(\mathbf{r})]\phi(\mathbf{r},\mathbf{k}) = \mathrm{E}(\mathbf{k})\phi(\mathbf{r},\mathbf{k}) \tag{2.4}$$

are given by:

$$\phi(\mathbf{r},\mathbf{k}) = \mathbf{e^{jk\cdot r}U_n}(\mathbf{r},\mathbf{k}), \tag{2.5}$$

with $U_n(\mathbf{r},\mathbf{k})$ periodic with the periodicity of the direct lattice, n the band index and j the negative square root of minus one. [6] This solution to the Schrödinger equation is known as the Bloch function, which is periodic with the lattice, for all direct lattice vectors $\mathbf{R}$, in mathematical form:

$$\phi(\mathbf{r}+\mathbf{R},\mathbf{k}) = \mathbf{e^{jk\cdot r}e^{jk\cdot R}U_n}(\mathbf{r},\mathbf{k}). \tag{2.6}$$

It can also be shown that the energy $E(\mathbf{k})$ is periodic in the reciprocal lattice for all reciprocal lattice vectors $\mathbf{G}$, in other words:

$$E(\mathbf{k}) = E(\mathbf{k}+\mathbf{G}). \tag{2.7}$$

To label the energy uniquely for a given band index, it is sufficient to only use wave vectors in the first Brillouin-zone, which is known as the Wigner-Seitz cell in the reciprocal lattice. The Wigner-Seitz cell can be constructed by drawing perpendicular bisector planes in the reciprocal lattice from the chosen centre to the nearest equivalent reciprocal lattice sites. [7] From this it is evident that any wave vector in the reciprocal lattice can be reduced to a point in the Brillouin-zone. [8]

Energy bands have been studied extensively, and in semiconductors physics there are three methods frequently used namely: orthogonal plane-wave method, pseudo-potential method and the $\mathbf{k}\cdot\mathbf{p}$ method. [4] [9] In Figure 2.3 the band structures for silicon and germanium are shown. Notice from the graph that there is a forbidden region, in this region energy states are forbidden, above and below this region are the allowed states. The upper region is known as the conduction band, whereas the lower region is the valence band. The energy range between the lowest conduction band state and highest valence band state is known as the band gap. Every energy state is characterised by a specific wave vector. If the wave vector for the lowest energy state in the conduction band is the same as for the highest energy state in the valence band, then it is called a direct band gap, otherwise it is called an indirect band gap. In Figure 2.3 it shows that silicon and germanium have an indirect band gap whereas gallium arsenide has a direct band gap, therefore it can easily emit light.

Near the top of the valence band and bottom of the conduction band at Γ we see a splitting of the bands, this is due to spin-orbit interaction. Here, the bands can be approximated using a quadratic equation which satisfies:

$$\frac{1}{m_{ij}^*} = \frac{1}{\hbar^2}\frac{\partial^2 E(\mathbf{k})}{\partial k_i \partial k_i}, \tag{2.8}$$

with m_{ij}^* the associated effective mass.

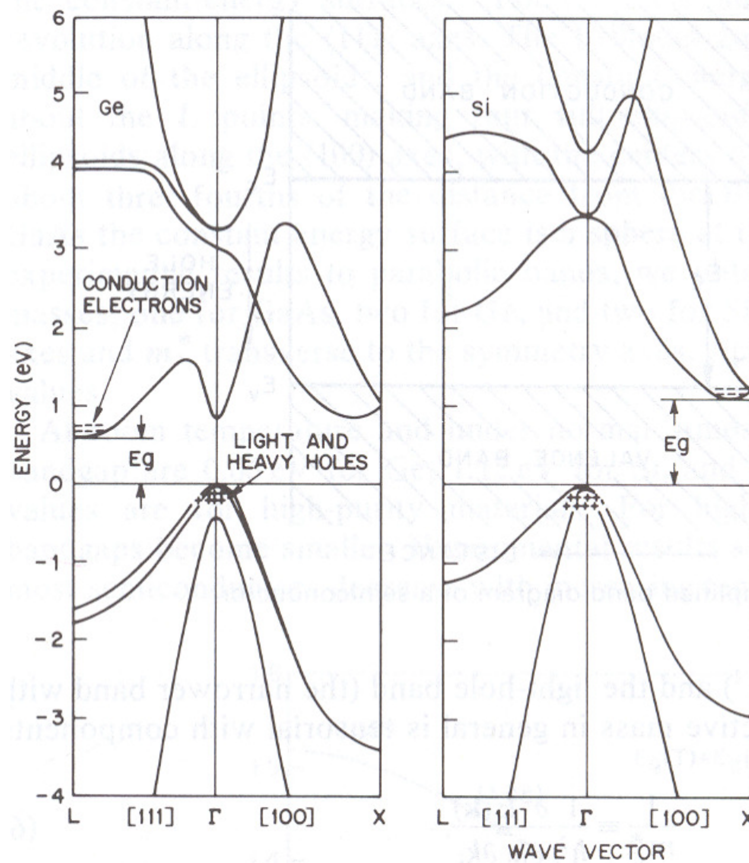

FIGURE 2.3: Energy band diagram for silicon and germanium. [4]

As mentioned earlier, each atom has four valence electrons bonded covalently to four nearest neighbour atoms. For a pure semiconductor at absolute zero these electrons will occupy all of the available energy levels within the valence band, whereas the conduction band will be completely empty, thus no conduction can take place. For temperatures above absolute zero, thermal excitation happens, and electrons are excited from the valence band into the conduction band, where they are free to migrate throughout the lattice. The energy required to promote and electron from the valence band to the conduction band is equal to the band gap energy. The band gap energy can be approximated at different temperatures by the following equation:

$$E_g(T) = E_g(0) - \frac{\alpha T^2}{(T+\beta)}, \tag{2.9}$$

with α and β material dependent constants. [4] Given the constants and knowing the band gap energy at absolute zero we can determine the band gap energy at any specific temperature. Given in Table 2.1 are the band gap energies for silicon, germanium and gallium arsenide at absolute zero and at room temperature as well as the necessary coefficients.

TABLE 2.1: Band gap energy for some semiconductors at absolute zero and at room temperature.

Material	$E_g(0)$ eV	$E_g(300)$ eV	α 10^{-4}eV/K	β K
Silicon	1.17	1.12	4.73	636
Germanium	0.74	0.66	4.77	235
Gallium arsenide	1.52	1.42	5.41	204

When an electron is excited to the conduction band, it leaves behind a positive charge inside the valence band called a hole, which is also free to migrate throughout the crystal, thus excitation of an electron forms an electron-hole pair. A hole can be seen as an electron with a positive charge, which contributes to the conductivity of the material, this will be shown in the next section.

Table 2.2 shows the electron and hole mobility for three most common semiconductors. The mobility is a measure of how quickly the charge carrier can move through the solid, and will be used later in this study.

TABLE 2.2: Electron and hole mobility for some semiconductors at room temperature.

Material	μ_e $\mathrm{cm}^2/\mathrm{Vs}$	μ_h $\mathrm{cm}^2/\mathrm{Vs}$
Silicon	1500	450
Germanium	3900	1900
Gallium arsenide	8000	400

2.5 Carrier Concentration at Thermal Equilibrium

The energy of an electron in the lowest energy state of the conduction band is denoted by E_C and a hole in the highest energy state of the valence band is denoted by E_V, and the band gap are denoted by E_g. One can think of E_V as the highest energy electrons can occupy at 0 K, while E_C is the the lowest vacant electronic states. The density of states per unit volume per unit energy is then defined as:

$$N(E) = \frac{d\Gamma(E)}{dE}, \tag{2.10}$$

with $\Gamma(E)$ the total number of states up to an energy E per unit volume. Assuming that the bands are parabolic, [4] which means that the energy relates to the momentum quadratically, it may be shown that the density of states for the conduction band can be written as:

$$N_C(E) = 6(4\pi h^{-3})(2m_n^*)^{\frac{3}{2}}(E - E_C)^{\frac{1}{2}}, \tag{2.11}$$

and in the same way, the density of states for the valence band are:

$$N_V(E) = 6(4\pi h^{-3})(2m_p^*)^{\frac{3}{2}}(E_V - E)^{\frac{1}{2}}, \tag{2.12}$$

with h Plank's constant, m_n^* and m_p^* the density of state effective masses for electrons and holes respectively. [3] We are now in a position to calculate the carrier concentration in the valence and conduction bands as a function of the Fermi energy.

2.5.1 Intrinsic Case

The density of occupied conduction band states is given by:

$$\begin{aligned} n &= \int_{E_C}^{\infty} N_C(E)F(E)dE \\ &= \int_{E_C}^{\infty} N_C(E)(1+\exp(\frac{E-E_F}{k_BT}))^{-1}dE, \end{aligned} \tag{2.13}$$

where $F(E)$ is the Fermi-Dirac distribution function for electrons in the conduction band, with k_B Boltzmann's constant, E_F the Fermi energy and T the absolute temperature. [3] [4] Evaluating the integral from the bottom of the conduction band to infinity, we obtain the density of free electrons in the conduction band as:

$$n = N_C \exp(-\frac{E_C - E_F}{k_BT}), \tag{2.14}$$

where N_C is the effective density of states in the conduction band given by:

$$N_C = 2(\frac{2\pi m_n^* k_B T}{h^2})^{\frac{3}{2}}. \tag{2.15}$$

Similarly, we can find the density of free holes in the valence band as:

$$p = N_V \exp(-\frac{E_F - E_V}{k_BT}), \tag{2.16}$$

where N_V is the effective density of states in the valence band given by:

$$N_V = 2(\frac{2\pi m_p^* k_B T}{h^2})^{\frac{3}{2}}. \tag{2.17}$$

When we refer to an intrinsic semiconductor, we mean semiconductors which is free of any impurity atoms, or at least a negligible amount of impurities. Since the semiconductor does not contain any impurities and is not charged we can conclude that the number of holes and electrons are equal, such that:

$$n = p = n_i. \tag{2.18}$$

Now, by equating Equations 2.14 and 2.16 the Fermi energy of the intrinsic semiconductor may be found as:

$$E_F = E_i = \frac{E_C + E_V}{2} + \frac{k_BT}{2}\ln(\frac{N_V}{N_C}). \tag{2.19}$$

By using Equations 2.15, 2.17 and 2.19 the intrinsic carrier density can be found to be equal to:

$$n_i = \sqrt{N_V N_C}\exp(-\frac{E_g}{2k_BT}). \tag{2.20}$$

It follows that for non-degenerate semiconductors that the product of minority and majority carrier concentrations are fixed, in mathematical form:

$$np = n_i^2 = N_C N_V \exp(-\frac{E_g}{k_B T}). \tag{2.21}$$

Note that an increase in the band gap energy decreases the intrinsic carrier density, whereas an increase in temperature increases the intrinsic carrier concentration. When the band gap increases the electrons require more energy to cross the band gap into the conduction band, thus when the temperature is increased the electrons acquire the needed energy, and so the carrier concentration increases. [10] [4]

2.5.2 Extrinsic Case

We now refer to the case where the semiconductor has been doped with impurity atoms. Doping is the process in which known amounts of impurity atoms have been intentionally added to the pure semiconductor. A doped semiconductor is referred to as an extrinsic semiconductor. There is two possibilities when doping a Group IV semiconductor with impurities, either by Group III or Group V elements, both of these cases will be discussed.

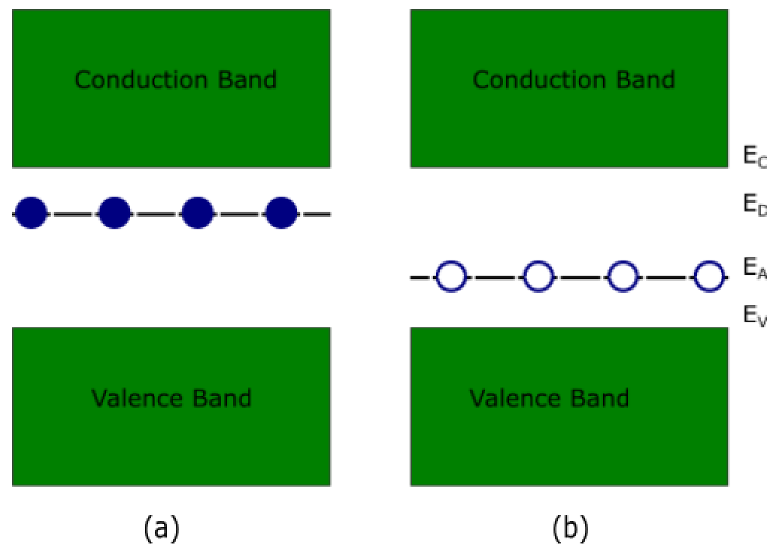

FIGURE 2.4: Energy-band diagram showing when: (a) donor impurity, and (b) acceptor impurity atoms have been added.

Firstly, consider the case when a Group V element is added to the semiconductor, these elements contain five valence electrons, four of which will contribute to the covalent bonds, leaving one loosely bound electron. These loosely bound electrons are referred to as donor electrons, and the impurity atoms as donor atoms. Increasing the temperature gives the electrons the required energy to jump into the conduction band, and move freely throughout the lattice. Doping with donors therefore produces a level E_D close to the conduction band, as shown in Figure 2.4 (a). This type of material is referred to as an n-type semiconductor. From Equation 2.14, 2.18 and using E_i as the reference energy we can determine the density of free electrons in

the conduction band for n-type semiconductor to be:

$$n = n_i \exp(-\frac{E_F - E_i}{k_B T}). \quad (2.22)$$

Now consider the case when a Group III element, with three valence electrons, is added to the semiconductor. Since there are only three valence electrons only three covalent bonds can be formed, leaving one empty covalent bond. Thus an electron can jump into this empty state and form a covalent bond, these empty states are called acceptors atoms, since they can accept electrons. The energy-band diagram for this case can be seen in Figure 2.4(b). The energy of these acceptor levels is denoted by E_A. At very low temperatures these states will remain empty, increasing the temperature gives the electrons in the valence band enough energy to jump into these acceptor states. When this happens, holes are formed in the valence band, which can move freely throughout lattice. This type of material is referred to as an p-type semiconductor. In the same manner, from Equation 2.16, 2.18 and using E_i as the reference energy we can determine the density of free holes in the valence band of a p-type semiconductor to be:

$$p = n_i \exp(-\frac{E_i - E_F}{k_B T}). \quad (2.23)$$

Ionisation Energy

The ionisation energy is defined as the minimum amount of energy required to remove the outer most loosely bound electron from an atom. [3] For hydrogen, the ionisation energy may be calculated using the Bohr model of the atom, which is given by:

$$E = \frac{m_0 q^4}{32\pi^2 \hbar^2 \epsilon_0^2}. \quad (2.24)$$

The ionisation energy for acceptor and donor atoms can also be calculated using this model, referred to as the hydrogenic model, as:

$$E = \frac{m^* q^4}{2(n\hbar)^2 (4\pi\epsilon_s)^2}, \quad (2.25)$$

where we have used ϵ_s the permittivity of the semiconductor, n is a positive integer, and m^* the conductivity effective mass. [4] It was found that the ionisation energy required to remove an electron from the donor atom into the conduction band to be equal to 0.025 eV and the ionisation energy required to remove a hole from the acceptor atom into the valence band to be equal to 0.050 eV. This shows that the ionisation energy for silicon is much less than that of the hydrogen atom, with an ionisation energy equal to 13.6 eV.

Carrier Concentration and Fermi Energy

When an extrinsic semiconductor is at thermal equilibrium the net charge density is zero. We consider the case, where donor impurities with concentration of N_D are added to the crystal. To preserve charge neutrality the total negative charges must equal the total positive charges, in mathematical terms:

$$n = N_D^+ + p, \quad (2.26)$$

with n the free electron density in the conduction band, and p the free hole density in the valence band, and finally N_D^+ is the number of ionised donors. In a similar manner, when acceptor impurities with concentration of N_A is added to the crystal we have the following charge neutrality condition:

$$p = N_A^- + n, \tag{2.27}$$

where N_A^- is the number of ionised acceptors. Equation 2.22 and 2.23 can be used to calculate the concentration of free electrons and holes for a given impurity concentration. At relatively elevated temperatures we can assume complete ionisation of acceptor and donor atoms, in this case the the charge neutrality equation becomes:

$$n + N_A = p + N_D. \tag{2.28}$$

The substitution of Equation 2.21, gives rise to a quadratic equation, this equation can be solved in terms of the electron concentration for n-type material at thermal equilibrium:

$$n = \frac{1}{2}[(N_D - N_A) + \sqrt{(N_D - N_A)^2 + 4n_i^2}]. \tag{2.29}$$

In the same manner we can find the hole concentration for p-type material at thermal equilibrium, again we assume full ionisation of the acceptor atoms, and solving the quadratic equation, leads to the hole concentration in p-type material:

$$p = \frac{1}{2}[(N_A - N_D) + \sqrt{(N_A - N_D)^2 + 4n_i^2}]. \tag{2.30}$$

Previously in Equations 2.14 and 2.16 we solved the electron and hole concentration at thermal equilibrium in the conduction and valence band respectively using Boltzmann statistics. Using these two equations and solving them in terms of energy we find that the Fermi-energy for n-type semiconductor is:

$$E_C - E_F = k_B T \ln\left(\frac{N_C}{N_D}\right), \tag{2.31}$$

similarly for p-type semiconductor:

$$E_F - E_V = k_B T \ln\left(\frac{N_V}{N_A}\right). \tag{2.32}$$

This shows that the Fermi level for n-type material is somewhere between the conduction band and the intrinsic Fermi level, and for p-type material it is between the valence band and the intrinsic Fermi level. In a p-type semiconductor electrons are called minority carriers and holes are called majority carriers, and vice versa in n-type semiconductors.

Figure 2.5 illustrates how the electron density with a fixed doping concentration inside an n-type semiconductor changes with temperature. Initially, at lower temperatures only a few of the donor atoms are ionised, but as the temperature is increased, the number of ionised impurity atoms increases, this is known as partial ionisation. This will continue until all of the impurity atoms are ionised at which point the electron density within the conduction band remains constant, this is known as the extrinsic case. Further increasing the temperature will give the electrons sufficient energy to cross the band gap into the conduction band from the valence band. This

is known as the intrinsic case, in which the electron density in the conduction band is dependent on the intrinsic carrier density and not the doping concentration. [3]

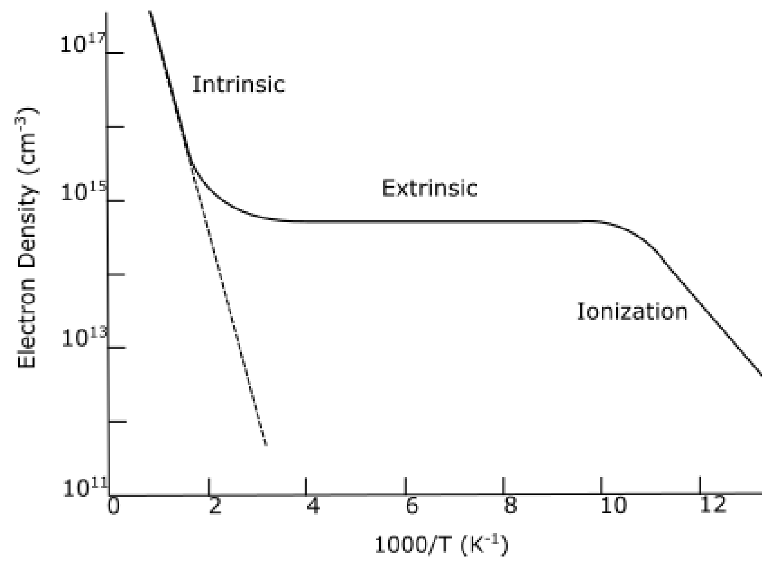

FIGURE 2.5: Electron density as function of temperature for n-type silicon. [10]

Chapter 3

Metal–Semiconductor Junctions

3.1 Introduction

The first rectifying properties were initially discovered by Ferdinand Braun as early as 1874, after which much research went into understanding metal–semiconductor contacts. In 1942 Schottky proposed a model which correctly described the phenomena. After this, rectifying metal–semiconductor junctions are often referred to as Schottky diodes. Schottky diodes are a very important part of the semiconductor industry, since they are often used in semiconductor devices, such as microwave reciever detectors, [11] gate electrodes in field-effect transistors. [4] They may also be used in studying defects introduced in semiconductors.

In Section 3.2 the formation of the ideal Schottky barrier for both p-type and n-type semiconductor will be discussed, and the effect of forward and reverse bias on the Schottky barrier height will be considered. The properties of the depletion region and all relevant equations will be derived. In Section 3.3 the various current transport mechanism through Schottky and Ohmic contacts will be explained. Finally, in Section 3.4 the formation of the Ohmic contact for an n-type semiconductor will be discussed.

3.2 Ideal Schottky Barrier

The formation of a Schottky barrier is illustrated in Figure 3.1. Initially the metal and semiconductor are isolated and then brought into contact. In the figure, $q\chi_s$ is the electron affinity of the semiconductor, the amount of energy released when an electron is added to the material. In other words the energy difference between the conduction band edge and the vacuum. The work function of a material is the minimum amount of energy needed to remove an electron from the material. Which is the energy difference between the Fermi-level and the vacuum, with $q\phi_m$ and $q\phi_s$ the work functions of the metal and semiconductor respectively. There are two possible cases, one in which $\phi_m > \phi_s$ and one in which $\phi_m < \phi_s$. In this section, we will consider the case $\phi_m > \phi_s$ for n-type material and $\phi_m < \phi_s$ for p-type material, as this leads to the formation of a Schottky diode. [12]

Consider the case for an n-type material $\phi_m > \phi_s$, as shown in Figure 3.1. Initially, the Fermi-level of the semiconductor is higher than that of the metal. When connected by a thin wire, electrons diffuse from the semiconductor to the metal. The only available electrons to diffuse from the semiconductor to the metal are from the conduction band, provided by the ionised donor atoms. This means that while the electrons accumulate on the surface of the metal, they leave behind positively

charged ionised donors some distance below the surface of the semiconductor. This region of uncompensated ionised donors is called the depletion region. [13] Due to the build-up of negative charges on the surface of the metal and positive charges beneath the surface of the semiconductor an electric field is formed across the depletion region, opposing the movement of electrons from the semiconductor to the metal. With the field, there is an associated electrostatic potential, which, when added to the energy of the bands, causes the bands in the semiconductor to bend upwards and the Fermi-level of the semiconductor to move closer to that of the metal. This process will continue until the Fermi-levels are aligned with each other.

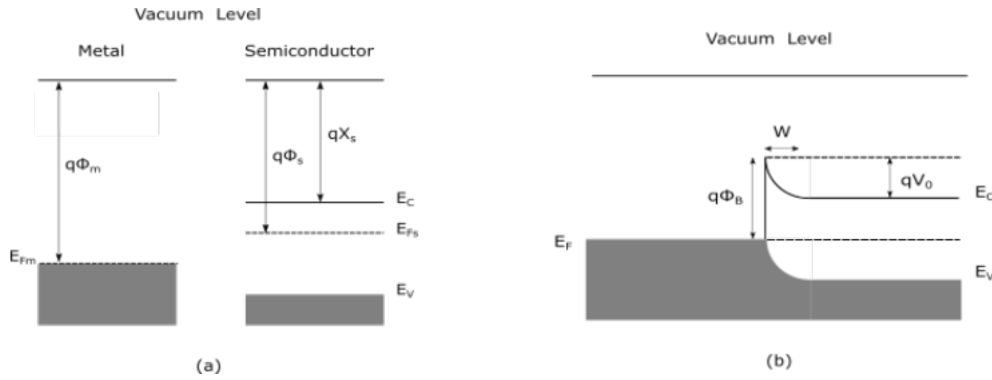

FIGURE 3.1: The formation of a metal and n-type semiconductor Schottky barrier: (a) metal and semiconductor in their isolated states, and (b) in intimate contact. [14]

The barrier seen by the electrons between the Fermi-level of the metal and the conduction band of the semiconductor as shown in Figure 3.1(b), is known as the Schottky barrier, with the height of the barrier measured relative to the Fermi level given by:

$$\phi_B = \phi_m - \chi_s. \tag{3.1}$$

The height of the barrier measured relative to the semiconductor conduction band is referred to as the built-in potential, and under zero bias conditions stated as:

$$V_0 = \phi_B - \xi, \tag{3.2}$$

where ξ is the energy difference between the Fermi level and the conduction band in the bulk. [4] By using charge neutrality it can be shown that:

$$\xi = k_B T \ln\left(\frac{N_C}{N_D}\right), \tag{3.3}$$

with N_C the effective density of states in the conduction band, and N_D the doping concentration. The effective density of states was derived in Chapter 2.5, and can be calculated using Equation 2.15.

Now, consider the case for a p-type material $\phi_m < \phi_s$, as shown in Figure 3.2. Initially the Fermi level of the metal will be greater than that of the semiconductor. When connected by a thin wire, electrons will diffuse from the metal to the semiconductor combining with holes in the valence band, which were provided by the ionised acceptor atoms. This means that while holes accumulate on the surface of the

metal, they leave behind negatively charge ionised acceptors some distance below the surface of the semiconductor. This region of uncompensated ionised acceptors is known as the depletion region. Due to the build-up of positive charges on the surface of the metal and negative charges beneath the surface of the semiconductor an electric field is formed across the depletion region attracting electrons within the conduction band of the semiconductor. Again, with this field, there is an accompanying electrostatic potential and when combined with the energy of the bands, causes the bands in the semiconductor to bend downwards and the Fermi level of the semiconductor to move closer to that of the metal. This process will continue until the Fermi levels are aligned with each other.

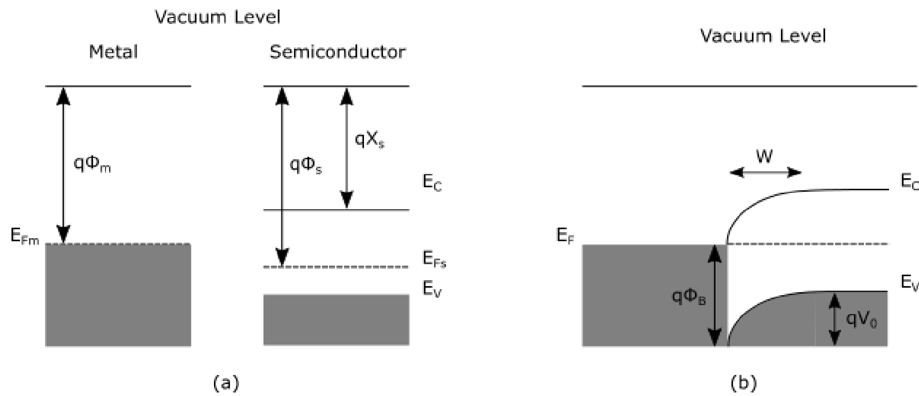

FIGURE 3.2: The formation of a metal and p-type semiconductor Schottky barrier: (a) metal and semiconductor in their isolated states, and (b) in intimate contact. [14]

With holes the majority carrier, the barrier seen by the holes due to the bending of the bands within the semiconductor, shown in Figure 3.2(b), is known as the Schottky barrier, with the height of the barrier measured relative to the Fermi level given by:

$$\phi_B = \frac{E_g}{q} - (\phi_m - \chi_s). \tag{3.4}$$

Here we have only considered the case for an ideal Schottky contact, but in practice it is almost impossible to form an ideal contact with conventional vacuum deposition without forming a thin oxide layer on the surface of the semiconductor. [4] Throughout the discussion it was also assumed that there does not exist interface states on the semiconductor, which is not always valid. For a more in depth discussion on these aspects influencing the barrier height refer to Rhoderick. [15]

3.2.1 Forward and Reverse Bias

Consider a metal contact on an n-type semiconductor as described earlier. When a zero bias is applied across the junction, electrons on both sides of the junction experience the same barrier height, measured relative to the Fermi level. Under these conditions there exists no net flow of electrons to and from the semiconductor. Now, if a forward bias (positive potential applied to the metal) is applied, it causes the Fermi level in the semiconductor to be raised relative to that of the metal. This decreases the amount of band bending and in turn reduces the barrier height experienced by the electrons in the semiconductor, while the barrier experienced by electrons in the

metal remains the same. As a result, a net flow of electrons from the semiconductor to the metal will exist, increasing the forward bias will increase the net flow of electrons and thus the current flowing through the junction. [16] With an applied potential V_D, the barrier height experienced by the electrons in the semiconductor is:

$$V_0 = \phi_B - \xi - V_D. \tag{3.5}$$

If a reverse bias (negative potential applied to the metal) is applied, the Fermi level in the semiconductor is now lowered relative to that of the metal. When this happens the bands tend to bend more, increasing the barrier height and depletion region width. The barrier height experienced by the electrons within the semiconductor is raised, but remains constant for electrons in the metal. Thus the current from the metal to the semiconductor remains constant, whereas the current from the semiconductor to the metal decreases as the reverse bias is increased, implying that the current tends to a finite value. This will continue until the electric field across the depletion region is large enough to cause dielectric breakdown of the semiconductor, which will cause a large current to flow through the junction. [13]

3.2.2 Depletion Region

In the previous section the relationship between the valence- and conduction bands of the semiconductor and the Fermi level of the metal at the interface, was discussed. This can be used as boundary condition for solving Poisson's equation in the semiconductor. Choosing the x-axis pointing into the semiconductor with $x = 0$ to be at the interface, the boundary conditions can be defined as $V(0) = V_0$ and $E(\infty) = 0$. Poisson's equation gives:

$$\frac{d^2V}{dx^2} = \frac{1}{\epsilon_s}\rho(x), \tag{3.6}$$

with $\rho(x)$ the total charge density at a depth x into the semiconductor and ϵ_s the permittivity of the semiconductor. [17]

The calculations are frequently simplified using the depletion region approximation. According to this approximation, an abrupt boundary between the depletion region (with no free charge carriers) and the bulk of the semiconductor (with $\rho = 0$ and $E = 0$) is assumed. This is equivalent to approximating the Fermi-Dirac distribution with a step function. Also ignoring any contributions from the valence band, band gap, conduction band and deep levels. If the width of the depletion region is w, the charge density within the semiconductor can be expressed as:

$$\rho(x) = \begin{cases} qN_D & \text{for} \quad x \leq w \\ 0 & \text{for} \quad x > w, \end{cases} \tag{3.7}$$

with N_D the doping concentration, and q the electronic charge. By double integration of Equation 3.6, and applying the boundary conditions previously mentioned, we obtain the width of the depletion region to be:

$$w = \sqrt{\frac{2\epsilon_s}{qN_D}(V_0 - \frac{k_BT}{q})}. \tag{3.8}$$

Applying a bias across the junction will adjust the depletion region width as follows:

$$w = \sqrt{\frac{2\epsilon_s}{qN_D}(V_0 - V_D - \frac{k_B T}{q})}, \tag{3.9}$$

where the temperature dependent term in Equation 3.8 is due to the majority-carrier distribution tail. [4] Thus the width of the depletion region is directly proportional to the square root of the applied potential, and inversely proportional to the square root of the doping concentration. Single integration of Equation 3.6 gives the electric field in the depletion region as:

$$E(x) = -\frac{qN_D}{\epsilon_s}(w - x). \tag{3.10}$$

With the maximum of the magnitude of the electric field found at $x = 0$. Integration of Equation 3.10 yields the electrostatic potential within the depletion region:

$$V(x) = -\frac{qN_D}{2\epsilon_s}(w - x)^2. \tag{3.11}$$

The charge per unit area in the depletion region, is equal to the doping concentration times the depletion width:

$$Q = qwN_D \tag{3.12}$$

$$= \sqrt{2q\epsilon_s N_D(V_0 - V_D - \frac{k_B T}{q})}. \tag{3.13}$$

Now that the charge per unit area is known within the semiconductor, it is possible to calculate the capacitance across the depletion region. [4] The capacitance per unit area is given by:

$$C = \frac{|\partial Q|}{\partial V_0} \tag{3.14}$$

$$= \sqrt{\frac{q\epsilon_s N_D}{2(V_0 - V_D - \frac{k_B T}{q})}}. \tag{3.15}$$

3.3 Current Transport Mechanisms

The current transport mechanisms in metal-semiconductors are mainly due to majority carriers passing through or across the potential barrier. These current transport mechanisms can be divided into four processes, namely:

(1) Transport of majority carriers over the potential barrier, known as thermionic-emission. This is usually the case for moderately doped semiconductors.

(2) Quantum-mechanical tunnelling through the potential barrier into the metal. This is important for highly doped semiconductors.

(3) Generation and recombination of carriers in the space-charge region. This will be discussed in more detail in the following chapter.

(4) Injection of minority carriers from the metal into the semiconductor.

In addition to the four mechanisms mentioned, there also exists leakage current due to a high electric field at the contact region or current due to traps at the metal-semiconductor interface. Figure 3.3 gives an illustration of these four current transport mechanisms under forward bias, with the inverse processes occurring under reverse bias.

The emission of charge carriers from the semiconductor across the barrier into the metal can be divided into two processes. In the first process the charge carriers are transported from the bulk of the semiconductor through the depletion region by means of drift and diffusion due to the electric field of the barrier. The second process, the emission of charge carriers from the semiconductor to the metal is determined by the rate at which charge carriers are able to go across the barrier. Both of these processes may be described by the diffusion theory and thermionic-emission theory. [18] [11] According to the diffusion theory the first process is the current-limiting process, whereas with the thermionic-emission theory the assumption is that the current-limiting process is the actual transfer of charge carriers across the barrier. For moderately doped silicon, the dominant current transport mechanism for reverse and forward bias is thermionic-emission. For this reason thermionic emission will be discussed shortly, but for a more detailed discussion about current transport mechanisms refer to Sze. [4]

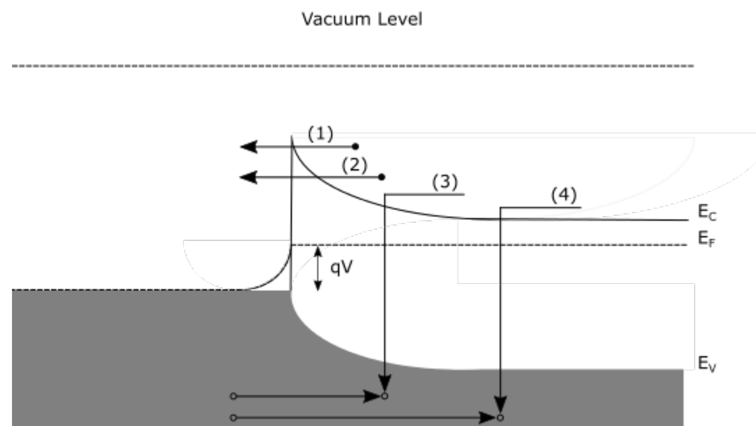

FIGURE 3.3: Current transport mechanisms under forward bias: (1) thermionic emission, (2) quantum-mechanical tunnelling, (3) generation and recombination of carriers, and (4) injection of minority carriers. [4]

Thermionic Emission

Thermionic emission theory is based on the assumptions that the barrier height is much larger than $k_B T$, thermal equilibrium is established at an interface that determines emission, and finally that the existence of a net current flow does not affect the equilibrium, so that one can superimpose two current fluxes, one from the semiconductor to the metal and from the metal to the semiconductor. [4] Thus the current density from the semiconductor to the metal are electrons with sufficient energy to

overcome the barrier, and can be calculated to be:

$$J_{s->m} = A^*T^2\exp(-\frac{q\phi_B}{k_BT})\exp(\frac{qV}{k_BT}), \tag{3.16}$$

where

$$A^* = \frac{4\pi qm^*k^2}{h^3}, \tag{3.17}$$

is the effective Richardson constant for thermionic emission.

Since the barrier height for electrons moving from the metal to the semiconductor is unaffected by the applied voltage the current flowing into the semiconductor also remains unaffected by the applied voltage. It must therefore be that the current flowing from the metal into the semiconductor must be equal to the current in the opposite direction when the applied potential is equal to zero. Using Equation 3.16 but with zero applied bias the current density from metal to semiconductor becomes:

$$J_{m->s} = -A^*T^2\exp(-\frac{q\phi_B}{k_BT}). \tag{3.18}$$

The total current density can now be given as the sum of Equations 3.16 and 3.18 as:

$$J_n = A^*T^2\exp(-\frac{q\phi_B}{k_BT})[\exp(\frac{qV}{k_BT}) - 1] \tag{3.19}$$

$$= J_s[\exp(\frac{qV}{k_BT}) - 1], \tag{3.20}$$

where J_s is referred to as the saturation current density, and is given by:

$$J_s = A^*T^2\exp(-\frac{q\phi_B}{k_BT}). \tag{3.21}$$

With Equation 3.20 corresponding to ideal contacts and needs to be adapted for various deviations from ideality. [4]

3.4 Ohmic Contacts

Ohmic contacts are defined as metal-semiconductor contacts, with negligible contact resistance when compared to the bulk of the semiconductor, resulting in a sufficiently small voltage drop across the contact even for larger currents. This should be the same under forward bias as well as reverse bias.

To achieve a low contact resistance, one of the methods could be to use metal–semiconductor combinations resulting in a low barrier height compared to k_BT. When this is the case, the charge carriers are now able to move more freely across the barrier in either direction, as shown in Figure 3.4(a). But due to the presence of interface states on the semiconductor, and metals having work functions that are too high, this means of creating ohmic contacts is not possible for n-type silicon.

There exists another more practical method for creating an ohmic contact with low contact resistance by means of tunnelling as shown in Figure 3.4(b). This is possible when the contact is formed on highly doped regions of the semiconductor. This

causes the barrier between the metal and semiconductor interface to be very narrow allowing charge carriers to tunnel through. [13]

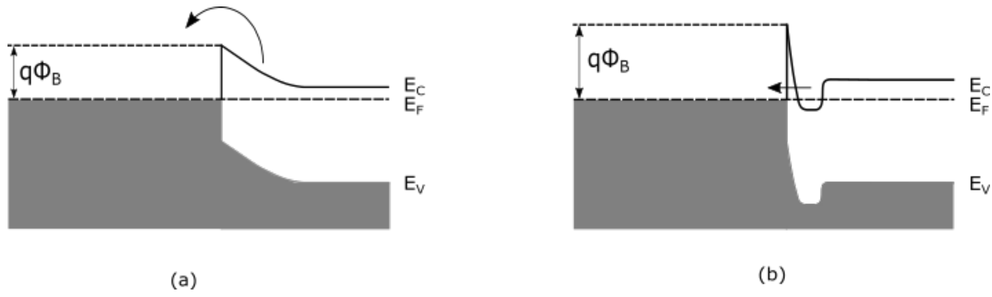

FIGURE 3.4: The formation of a metal and n-type semiconductor Ohmic contact: (a) low barrier height, and (b) high doping concentration. [4]

As mentioned, ohmic contacts has negligible contact resistance R_C compared to the bulk of the semiconductor, if measured at zero bias, the contact resistance is defined as:

$$R_C = (\frac{\partial J}{\partial V})^{-1}_{V=0}. \tag{3.22}$$

For low doping concentrations, the thermionic-emission current will dominate the current transport, ignoring the small voltage dependence of the barrier height, gives the contact resistance to be:

$$R_C = \frac{k}{qA^*T}(\frac{q\phi_B}{k_B T}). \tag{3.23}$$

However, for high doping concentrations, tunnelling will dominate. In this case the contact resistance is given by:

$$R_C = \exp\frac{2\sqrt{\epsilon_s m^*}}{\hbar}(\frac{q\phi_B}{\sqrt{N_D}}). \tag{3.24}$$

For a moderate doping concentrations the contact resistance is mostly due to the tunnelling process, and decreases rapidly with increasing doping concentration. Thermionic emission dominates for doping concentration less than 10^{17}cm^{-3}.

Thus in order to obtain a low contact resistance one should have a high doping concentration, a low barrier height or both. For semiconductors with wider bandgaps, it is not always possible to form an Ohmic contact, since there does not exist a metal with a low enough work function. In this case, high doping is used to form the Ohmic contact.

Chapter 4

Defects in Semiconductors

4.1 Introduction

Imperfections in the crystal lattice which cause any discontinuity are known as a defects, and may be introduced during some stage of crystal growth, fabrication process of semiconductor devices or irradiation. It is important to know which defects are introduced and present in semiconductors, since these defects alter the electronic properties of the material by allowing new energy states within the band gap.

Defects may be classified as point, line, planar and bulk defects. A point defect may be described as an imperfection at a single lattice site. [19] Some of the more common point defects are shown in Figure 4.1, and listed below:

- Vacancy: Lattice site missing an atom which is normally occupied.
- Self-interstitial: An atom occupying a lattice site which would normally not be occupied.
- Interstitial impurity: Impurity atom occupying a lattice site which would normally not be occupied.
- Substitutional impurity: Lattice site which is normally occupied by a host atom but in this case with an impurity atom.

Line defects are classified as a one-dimensional defects, since a line defect exists when there exists an imperfection in an entire row of lattice sites. [20]

Planar defects are two dimensional defects, which exists when an entire plane consists of imperfections, whereas a bulk defect is a three dimensional defect that exists over a volume within the crystal. [21]

In this chapter we start with describing the type of point defects found in semiconductors, the formation of point defects and clusters initiated by the interaction of high energy particles with the crystal structure. Subsequently, these defects are described under various equilibrium and non-equilibrium conditions.

4.2 Defect Generation

When a semiconductor is irradiated by energetic particles with an energy higher than the displacement threshold energy (the minimum kinetic energy needed to permanently displace an atom in a solid) it can displace atoms from normally occupied

lattice sites, thus creating a vacancy (V) and interstitial (I) pair, known as a Frenkel pair, as shown in Figure 4.1(e).

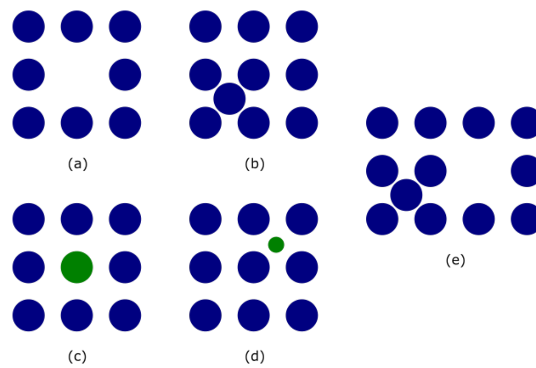

FIGURE 4.1: Illustrates some of the point defects: (a) vacancy, (b) interstitial, (c) impurity substitution, (d) impurity interstitial and (e) Frenkel pair. [22]

These displaced atoms are mobile at room temperature, and are able to move throughout the crystal structure. If the imparted energy of the primary knocked-on atom is high enough it is able to knock out other atoms in the crystal structure imparting some of its energy to the new knocked-on atom, forming defect cascades. [23] This will continue until the energy of the knocked-on atoms is lower than the displacement threshold energy, thus creating a region with a very high concentration of vacancies and interstitials. These regions are known as clusters. Figure 4.2 illustrates a simulation of the spatial distribution of vacancies in the crystal lattice after irradiation with neutrons.

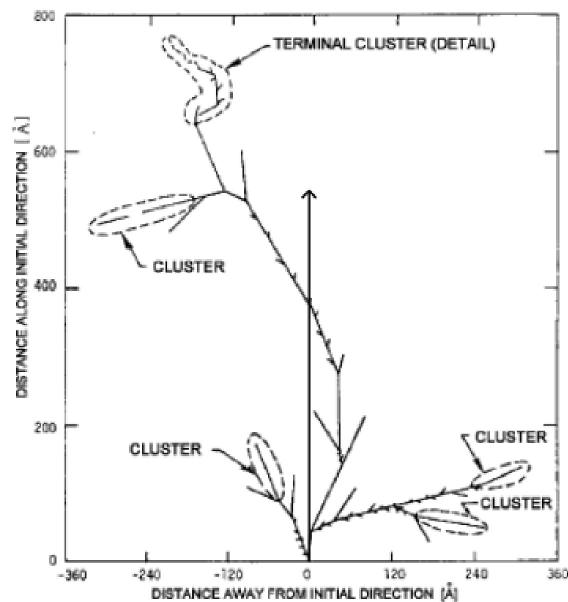

FIGURE 4.2: Simulation of the spatial distribution of vacancies formed after irradiation with neutrons. [24]

After irradiation, recombination between vacancy-interstitial pairs will occur, only if the distance between the vacancy and interstitial is less that the lattice constant. It is shown that more than half of the overall pairs generated undergoes recombination. [25] The rest of these vacancies and interstitials diffuse through the crystal lattice and react with themselves or with impurity atoms as shown in Figure 4.1, forming new point defects. The point defects and clusters formed during and after irradiation are the defects that are observed in the semiconductor, and their properties cause the observed change in microscopic and macroscopic properties of the semiconductor.

4.3 Classification of Defects

In the previous section it was mentioned that, when semiconductors are irradiated with energetic particles, there are predominantly point defects and clusters generated. This section is devoted to discuss the types and properties of clusters and point defects in semiconductors.

4.3.1 Clusters

In order to explain the very high minority carrier recombination rate observed after irradiation with heavy particles compared to that observed after gamma or electron irradiation, the cluster model was proposed. [26] Besides their composition of vacancies and interstitial no information about their exact nature or their electrical properties within the space charge region or under thermal equilibrium is known.

4.3.2 Point Defects

In Figure 4.3 some point defects found in silicon are shown, with their relative position in the forbidden band gap with respect to the valence and conduction band.

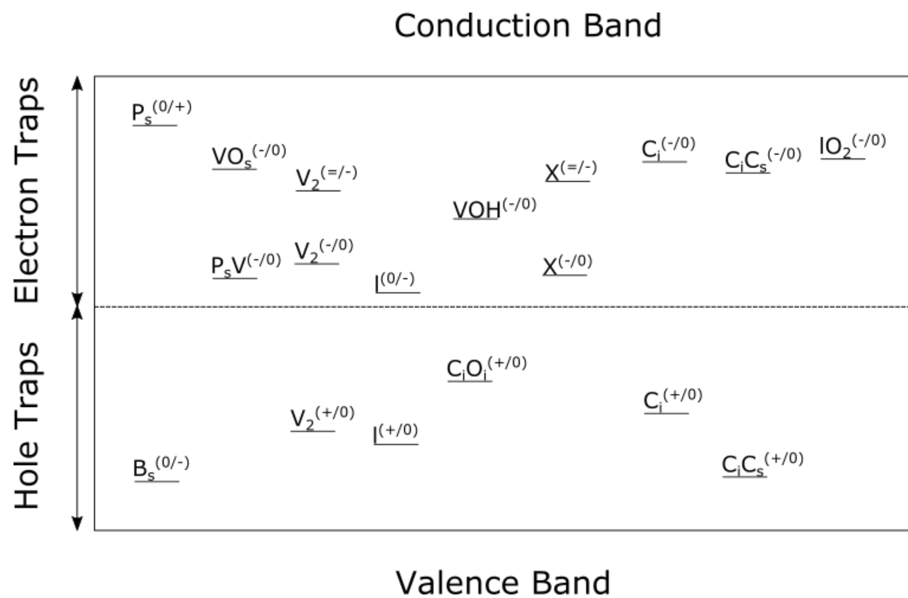

FIGURE 4.3: Observed point defects in the band gap of silicon. [27]

Acceptors, Donors and Amphoteric Defects:

Some of the defects created may be electrically active and contain energy levels within the forbidden band gap, which are able to capture or emit electrons and holes. If the energy of a defect state is denoted by E_T, in terms of the band edges, the energy may be defined as $E_T = E_C - E_A$ for defects in the upper half of the band gap, and as $E_T = E_V + E_A$ for defects in the lower half of the band gap. [28] In each of these equations E_A is the energy required to emit an electron into the conduction band or a hole into valence band.

When the semiconductor is in thermal equilibrium the charge of the defect state in the band gap depends on the Fermi level of the semiconductor. Acceptors are defined as being negatively charge when occupied by an electron and neutral when occupied by a hole, whereas donors are defined as being neutral when occupied by an electron and positive when occupied by a hole. Thus if the Fermi level is below the energy of the defect state, then acceptors will be neutral and donors will be positively charged, and if the Fermi level is above the energy of the defect state then acceptors will be negatively charged and donors will be neutral. Figure 4.3 depicts defect states that have both a donor and an acceptor level in the band gap, these defects are termed amphoteric.

Shallow and Deep Levels:

As mentioned previously, semiconductors may be doped with acceptor or donor impurity atoms, where acceptor levels are located close to the valence band and donor levels close to the conduction band. These defects are sometimes termed shallow levels, since they are close to the band edges in the forbidden band gap. Where deep-levels on the other hand are closer to the middle of the forbidden band gap.

Majority and Minority Carrier Traps:

It is often helpful to divide defect states into two groups, namely majority and minority carrier traps. It is termed a majority carrier trap if the thermal emission rate for majority carriers is much greater than the thermal emission rate for minority carriers, and vice versa for minority carrier traps.

4.4 Electrical Properties of Point Defects

This section is used to describe the occupation of traps with electrons and holes under various equilibrium conditions. Afterwards, the rate at which these traps are introduced and removed by means of annealing will be discussed.

4.4.1 Occupation of Traps at Thermal Equilibrium

Previously the Fermi-Dirac distribution function was used to determine the number of occupied states in the conduction and valence band at thermal equilibrium. It is also possible to use the Fermi-Dirac distribution function to determine the occupation of traps with electrons or holes for a non-degenerate semiconductor. The

Fermi-Dirac distribution function is defined as:

$$F(E) = 1 + \exp(\frac{E - E_F}{k_B T}). \tag{4.1}$$

If the total trap concentration is N_T, and the traps have an energy of E_T, the number of occupied traps with electrons is found to be:

$$\begin{aligned} n_T &= N_T F(E_T) \\ &= \frac{N_T}{1 + \exp(\frac{E_T - E_F}{k_B T})}. \end{aligned} \tag{4.2}$$

Similarly, the number of occupied traps with holes is:

$$\begin{aligned} p_T &= N_T(1 - F(E_T)) \\ &= \frac{N_T}{1 + \exp(-\frac{E_T - E_F}{k_B T})}. \end{aligned} \tag{4.3}$$

These quantities obey the totality condition:

$$N_T = n_T + p_T, \tag{4.4}$$

as each trap is either occupied by an electron or hole.

4.4.2 Energy and Gibbs Free Energy

So far the energy term has only been used in an abstract sense, from a thermodynamic point of view it is actually called the Gibbs free energy. [29] The number of free electrons in the conduction band of a non-degenerate semiconductor may be written in terms of the Gibbs free energy:

$$n = N_C(-\frac{\Delta G}{k_B T}). \tag{4.5}$$

The Gibbs free energy can be described by two new thermodynamic variables as:

$$\Delta G = \Delta H - T\Delta S, \tag{4.6}$$

with ΔH the change in enthalpy and ΔS the change in entropy. The number of free electrons within the conduction band defined in terms of Gibbs free energy are:

$$n = N_C(-\frac{\Delta G}{k_B T}). \tag{4.7}$$

By using Equation 4.6, we can rewrite the number of free electrons within the conduction band in terms of enthalpy as:

$$n = X_n N_C(-\frac{\Delta H}{k_B T}), \tag{4.8}$$

with the temperature independent entropy factor defined as:

$$X_n = \frac{\Delta S}{k_B T}. \tag{4.9}$$

4.4.3 Carrier Recombination Processes

In indirect band-gap semiconductors the most dominant processes are single-level recombination processes, these processes are so called, since there only exists a single-level of localised energy states in the forbidden band-gap, known as traps. [4] Normally without these states present the probability of a transition from the valence band to the conduction band would be relatively low, due to the large energy difference between the valence and conduction band. With the introduction of these intermediate states the probability of a transition will be increased, due to the decreased energy difference between the valence and conduction band states. In Figure 4.4 these single-level recombination processes are illustrated. The top part of the Figure is before and the bottom part is after the recombination process.

Knowing all the possible transition processes from and to the traps, it is possible to determine the rate of change of the number of occupied traps, with electrons and holes respectively as:

$$\frac{dn_T}{dt} = r_a - r_b - r_c + r_d \quad \text{and} \quad \frac{dp_T}{dt} = -r_a + r_b + r_c - r_d, \tag{4.10}$$

where r_a is the rate of electron capture, r_b the rate of electron emission, r_c the rate of hole capture, and finally r_d the rate of hole emission. The only traps available for capturing an electron are those occupied by a hole, whereas the only available traps for hole capture are those occupied by electrons.

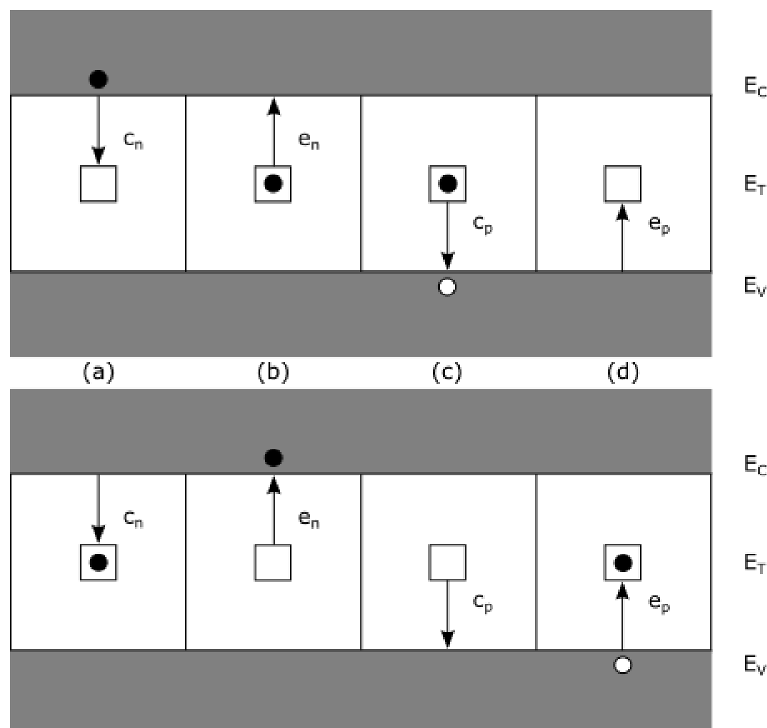

FIGURE 4.4: Single-level recombination processes for indirect band gap semiconductors: (a) electron capture, (b) electron emission, (c) hole capture, and (d) hole emission. With the top before recombination and the bottom after recombination. [30]

With the help of Equations 4.2 and 4.3 the rate of electron and hole capture can be expressed as:

$$r_a = c_n n(1 - F(E_T))N_T \quad \text{and} \quad r_c = c_p pF(E_T)N_T, \tag{4.11}$$

with c_n and c_p the capture rate for electrons and holes respectively. The only traps capable of electron emission are those occupied by an electron, and the only traps capable of hole emission are those occupied by a hole. Again, with the use of Equation 4.2 and 4.3 the rate of electron and hole emission can be expressed as:

$$r_b = e_n F(E_T)N_T \quad \text{and} \quad r_d = e_p(1 - F(E_T))N_T, \tag{4.12}$$

with e_n and e_p the emission rate for electrons and holes respectively. In thermal equilibrium the capture rates (r_a and r_c) and the emission rates (r_b and r_d) are equal, expressing the emission rate in terms of the capture rate for electrons and holes:

$$e_n = c_n n\frac{(1 - F(E_T))}{F(E_T)} \quad \text{and} \quad e_p = c_p p\frac{F(E_T)}{(1 - F(E_T))}. \tag{4.13}$$

Substitution of the Fermi-Dirac distribution function:

$$e_n = c_n n\text{exp}(\frac{E_T - E_F}{k_B T}) \quad \text{and} \quad e_p = c_p p\text{exp}(\frac{E_F - E_T}{k_B T}). \tag{4.14}$$

If it is assumed that there is no barrier to overcome during the capture process, then the probability per unit time with which a trap captures a charge carrier is:

$$c_n n = \sigma_n v_{th,n} n \quad \text{and} \quad c_p p = \sigma_p v_{th,p} p, \tag{4.15}$$

with $\sigma_{n,p}$ the capture cross section for electrons and holes respectively, and v_{th} the thermal velocity and may be expressed as:

$$v_{th,n} = \sqrt{\frac{8k_B T}{\pi m_e^*}} \quad \text{and} \quad v_{th,p} = \sqrt{\frac{8k_B T}{\pi m_h^*}}. \tag{4.16}$$

Finally, the emission rate for electron and holes is:

$$e_n = \sigma_n v_{th,n} N_C \text{exp}(\frac{E_T - E_C}{k_B T}) \quad \text{and} \quad e_p = \sigma_p v_{th,p} N_V \text{exp}(\frac{E_V - E_T}{k_B T}). \tag{4.17}$$

It is also common to write the emission rate in terms of thermodynamic properties introduced previously, substitution of Equations 4.8 into Equation 4.17 leads to:

$$e_n = c_n N_C X_n \text{exp}(-\frac{\Delta H}{k_B T}) \quad \text{and} \quad e_p = c_p N_V X_p \text{exp}(-\frac{\Delta H}{k_B T}). \tag{4.18}$$

Normally the capture rate is expressed in terms of the capture cross section: [4]

$$c_n X_n = \sigma_n v_{th,n} \quad \text{and} \quad c_p X_p = \sigma_p v_{th,p}. \tag{4.19}$$

Thus in terms of enthalpy, the emission rates are:

$$e_n = \sigma_n v_{th,n} N_C \text{exp}(-\frac{\Delta H_n'}{k_B T}) \quad \text{and} \quad e_p = \sigma_p v_{th,p} N_V \text{exp}(-\frac{\Delta H_p'}{k_B T}), \tag{4.20}$$

where the prime indicates the assumption that the capture cross section is independent of temperature, and hence remains constant.

4.4.4 Defect Occupation with Time

So far it was considered that the semiconductor is in thermal equilibrium. However, if the equilibrium is disturb there are processes that will attempt to restore the equilibrium. It is possible to describe the occupation of traps with respect to time in terms of the emission and capture rates. The occupation of traps with electrons and holes was previously expressed as:

$$\frac{dn_T}{dt} = r_a - r_b - r_c + r_d \quad \text{and} \quad \frac{dp_T}{dt} = -r_a + r_b + r_c - r_d. \tag{4.21}$$

After substitution of each term, and some rearrangement the rate of change of occupied traps is given by:

$$\frac{dn_T}{dt} = (c_n + e_p)(N_T - n_T) - (c_p + e_n)n_T$$

and

$$\frac{dp_T}{dt} = (c_p + e_n)(N_T - p_T) - (c_n + e_p)p_T. \tag{4.22}$$

It is possible to solve this differential equation in terms of the occupation of traps with time, but usually some assumptions are made. [17]

4.4.5 Defect Occupation under Bias

Semiconductors can be placed under a forward or reverse bias. When a reverse bias is applied to a diode, it increases the width of the depletion region, thus removing nearly all of the free charge carriers. When a forward bias is applied to a diode, a large number of free charge carriers are injected into the bulk of the semiconductor. [31] [28] Both these cases for negatively and positively doped semiconductors will be discussed briefly.

Reverse Bias:

When placed under reverse bias, in the depletion region there exists a non-equilibrium condition in which Equations 4.2 and 4.3 are no longer suitable to calculate the occupation of traps. Since the concentration of free charge carriers within the depletion region is very low, it is assumed that the capture rate of free charge carriers into traps is negligibly small, thus Equation 4.9 reduces to:

$$\frac{dn_T}{dt} = -r_b + r_d = -e_n n_T + e_p p_T$$

and

$$\frac{dp_T}{dt} = r_b - r_d = e_n n_T - e_p p_T. \tag{4.23}$$

Thus the occupation of traps with electrons and holes respectively, inside the depletion region is given by:

$$n_T = \frac{e_p}{e_n + e_p} N_T \quad \text{and} \quad p_T = \frac{e_n}{e_n + e_p} N_T. \tag{4.24}$$

For high radiation damage, the assumption that the free charge carriers within the depletion region is negligibly small, is invalid, and needs to be taken into account. Under these circumstances the occupation of traps with electrons and holes are thus:

$$n_T = \frac{c_n n + e_p}{e_n + c_p p + c_n n + e_p} \quad \text{and} \quad p_T = \frac{c_p p + e_n}{e_n + c_p p + c_n n + e_p}. \tag{4.25}$$

Forward Bias:

When placed under forward bias, electrons and holes are able to fill nearly all the traps in the bulk of the semiconductor. With this injection of free charge carriers we assume that the emission rate is negligibly small compared to the capture rate and in this case Equation 4.9 reduces to:

$$\frac{dn_T}{dt} = r_a - r_c = c_n n_T - c_p p_T. \tag{4.26}$$

Again, the occupation of traps with electrons and holes under forward bias is given by:

$$n_T = \frac{c_n n}{c_n n + c_p p} N_T \quad \text{and} \quad p_T = \frac{c_p p}{c_n n + c_p p} N_T. \tag{4.27}$$

Notice that a trap is only filled with an electron if the capture coefficient for holes are smaller than that of electrons, and is filled with a hole if the capture coefficient for electrons are smaller than that of holes.

4.5 Defect Introduction

Defect introduction kinetics describes the rate at which defects are introduced to the crystal lattice and what effect other defects has on the rate of introduction for a specific defect. Here the zeroth-order and first-order introduction rates will be discussed briefly. [31] [28]

4.5.1 Zeroth-Order

The zeroth-order introduction rate does not depend on the initial concentration of other radiation-induced defects present, the introduction rate also does not depend on increasing the concentration of other defects with time, in this instance the zeroth-order introduction rate can be given by:

$$k_1 = \frac{dN_{T_1}}{dt}, \tag{4.28}$$

with N_{T_1} and k_1 the concentration and introduction rate constant of defect one respectively. Integration of Equation 4.31 leads to:

$$N_{T_1}(t) = k_1 t + N_{T_1}(0), \tag{4.29}$$

where $N_{T_1}(0)$ is the initial concentration of defect one before any radiation, which is assumed to be zero. Thus Equation 4.29 shows that the concentration of defect one increases linearly with the duration of irradiation.

4.5.2 First-Order

Unlike the zeroth-order, the first-order introduction rate depends on the initial concentration of other defects present. Assume that there exists two defects, with the concentration of defect one denoted as N_{T_1} and the concentration of defect two denoted as N_{T_2}. Where the introduction rate of defect two is linearly dependent on concentration of defect one, and the concentration of defect one follows a zeroth-order introduction rate. Then the first-order introduction rate can then be written as:

$$N_{T_1} k_2 = \frac{dN_{T_2}}{dt}, \tag{4.30}$$

with k_2 the introduction rate constant of defect two. Integration of Equation 4.30 leads to:

$$N_{T_2}(t) = \frac{1}{2} k_1 k_2 t^2 + k_2 N_{T_1}(0) + N_{T_2}(0), \tag{4.31}$$

with $N_{T_1}(0)$ and $N_{T_2}(0)$ the initial concentration of defect one and two respectively. If it is assumed that the initial concentration is zero, then Equation 4.31 can be simplified to:

$$N_{T_2}(t) = \frac{1}{2} k_1 k_2 t^2. \tag{4.32}$$

This shows that the introduction rate of defect two is linearly dependent on defect one and increases quadratically with time. Figure 4.5 is a simulation that shows the concentration of defect one that follows the zeroth-order, the concentration of defect two that follows the first-order and the concentration that would be observed for both defects combined as a function of time. In the simulation it was assumed that the initial concentration for both defects to be zero. The introduction rate constants were arbitrarily chosen and to be equal.

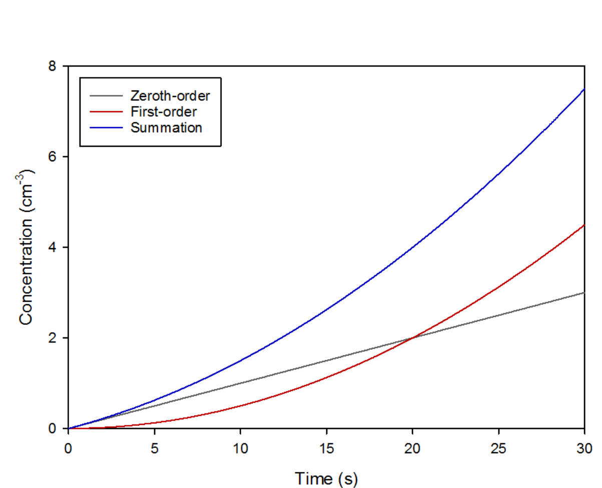

FIGURE 4.5: Simulation showing the concentration of defects following the zeroth-order and the first-order introduction rates, with the expected concentration of both defects combined.

4.6 Defect Annealing

Annealing is the process whereby heat treatment is applied to a material in order to change its physical or chemical properties. In the semiconductor industry, annealing is generally used to diffuse dopant atoms into substitutional positions inside the crystal lattice. It can also be used to remove some defects introduced during irradiation. In both these cases the electrical properties of the material is changed significantly. The mechanisms whereby defects are annealed and the rate at which the defects are annealed will be discussed.

4.6.1 Annealing Mechanisms

Mechanisms by which defects within the crystal lattice anneal can roughly be divided into three main categories, as defect migration, complex formation and complex dissociation.

Defect Migration and Complex Formation:

Increased temperature of the crystal lattice gives the defects sufficient energy to overcome the binding energy and move freely through the crystal, and will continue for as long as the temperature remains high enough. At some point the defects will be gathered at a sink, recombine with their counterparts or form new defects by association with same or a different type of defect.

Complex Dissociation:

A complex is a defect composed of more than one constituent. If the temperature is high enough so that the complexes obtains enough energy to overcome the binding energy they dissociate into their constituents. These constituents will migrate through the crystal lattice and form new defects or disappear into a sink.

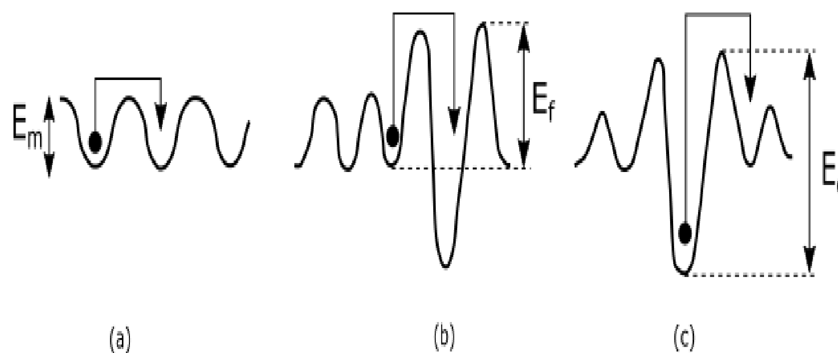

FIGURE 4.6: Illustrates the mechanism and corresponding activation energy: (a) defect migration, (b) complex formation, and (c) complex dissociation. [32]

Figure 4.6 is a schematic representation of all three mechanisms. It can be seen in the schematic that each of these processes are characterised by an activation energy (E_m, E_f, E_d), which is the energy needed to overcome the binding energy. With experimental results it is normally difficult to tell which of these processes is the

underlying cause for the observed changes, thus the term activation energy E_A will be used for all three cases in the mathematical formulation of the activation energy.

4.6.2 Reaction Rate

If the defects and complexes are randomly distributed throughout the crystal lattice, the rate at which defect migration and complex dissociation takes place can easily be described by a first order reaction. The number of defects combining with sinks or the number of complex dissociations that takes place per unit time is directly proportional to the number of defects or complexes present at that time, and can thus be written as:

$$-\frac{dN_T}{dt} = kN_T, \tag{4.33}$$

with N_T the defect concentration and k the annealing rate constant. [31] [33] The temperature dependence of this rate constant can be described by an Arrhenius relation:

$$k = k_0 \exp(-\frac{E_A}{k_B T}), \tag{4.34}$$

with k_0 the frequency factor, and E_A the activation energy for defect migration or complex dissociation. Where the frequency factor is related to the attempt-to-escape frequency, estimated by the most abundant phonon frequency. [34] In other words, the frequency factor may be expressed as:

$$k_0 = \delta \cdot \frac{k_B T}{h}, \tag{4.35}$$

where δ is an indication whether the observed reaction was due to defect dissociation ($\delta = 1$) or due to a long range defect migration ($\delta << 1$). The inverse of δ gives an approximation of the number of jumps necessary to remove a defect, but this only holds if the activation energy required for defect migration is smaller than the activation energy required for complex formation, refer to Figure 4.6. [31]

In Equation 4.33 the annealing rate was described in terms of a differential equation. For a first order reaction this equation can easily be solved to give the defect concentration at any given time as:

$$N_T(t) = N_T(0)\exp(-kt). \tag{4.36}$$

Taking the natural logarithm on both sides:

$$\ln \frac{N_T(t)}{N_T(0)} = -kt. \tag{4.37}$$

This shows that by plotting the natural logarithm of the normalised defect concentration versus time leads to a straight line, where the gradient represents the rate constant for a specific temperature. In a similar fashion Equation 4.37 can be rewritten as:

$$\ln k = \ln k_0 - \frac{E_A}{k_B T}. \tag{4.38}$$

Where the gradient in this case represents the activation energy and the intercept with the vertical axis the frequency factor. Equation 4.35 can then be used to determine the mechanism by which defect annealing occurs.

4.7 Electric Field Dependence

In Section 3.2.2 it was derived that there exists an electric field within the depletion region, which is directly proportional to the width of the depletion region. The magnitude of this intrinsic electric field can be shown to be:

$$\begin{aligned} |E(x)| &= -\frac{qN_D}{\epsilon_s}(w-x) \\ &= \sqrt{\frac{2qN_D}{\epsilon_s}(V_0 - V_D - \frac{k_BT}{q})} - \frac{qN_D}{\epsilon_s}x. \end{aligned} \tag{4.39}$$

The above equation shows that the intrinsic electric field in the depletion region may be enhanced by increasing the doping concentration or by increasing the applied bias. This electric field can sometimes be quite large and close to the dielectric breakdown field of the semiconductor. When a trap is placed within the depletion region this trap will experience this electric field, which in turn will influence the potential well considerably and may, therefore increase the emission rate of charge carriers from these traps.

The two mechanisms whereby the emission rates are increased due to an electric field are Poole-Frenkel or phonon-assisted tunnelling. Both of these mechanisms for a Coulombic potential (the one-dimensional case) well is shown in Figure 4.7, and will be discussed here briefly.

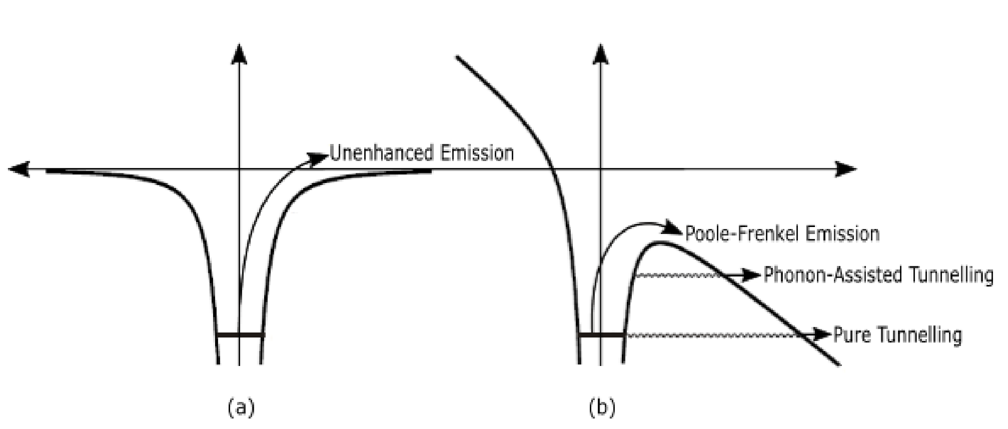

FIGURE 4.7: Illustrates a Coulombic potential well, with (a) no external electric field and (b) with an external electric field applied. [17]

4.7.1 Poole-Frenkel Effect

The simplest mechanism whereby the emission rate of charge carriers from a potential well is increased is known as the Poole-Frenkel effect and was first developed by Frenkel in 1938. [35] When an external electric field is applied to a charge carrier trapped in a potential well, the charge carrier will experience not only the intrinsic electric field but both of these fields combined, raising the potential barrier on the one side of the potential well and lowering the potential barrier on the other side, as shown in Figure 4.7.

For a Coulombic potential well placed in an external electric field, the lowering of the ionisation energy is given in the following form:

$$\Delta E_T = \sqrt{\frac{qF}{\pi\epsilon_s}}. \tag{4.40}$$

When substituted into Equation 4.17, the emission rate of charge carriers from a potential well under an external electric field can now be written as:

$$e(F) = e(0)exp(\frac{1}{k_B T}\sqrt{\frac{qF}{\pi\epsilon_s}}), \tag{4.41}$$

where $e(0)$ is the emission rate with no external electric field present and F the electric field strength. The Poole-Frenkel effect is the governing mechanism for shallow traps and where weaker electric fields are present. Equation 4.41 can now be used to determine if the enhanced emission is due to the Poole-Frenkel effect.

4.7.2 Phonon-Assisted Tunnelling

The second possible mechanism that will be discussed are phonon-assisted tunnelling or pure tunnelling, with the latter being more predominant in strong electric fields. It was found that traps having a significant electron-lattice coupling is likely to undergo phonon-assisted tunnelling. The coupling constant, which is also known as the Huang-Rhys factor, is different for every trap. [36] The coupling constant is represented by:

$$S = \frac{\Delta E}{\hbar\omega}, \tag{4.42}$$

with ΔE the vibrational energy loss. Due to this coupling electrons are able to occupy a set of stationary quasi-levels within the potential well, which are separated by the phonon energy. The emission rate of charge carriers from a potential well due to phonon-assisted tunnelling as described by Pons in 1979, [37] is given by:

$$e(F) = \sum_p \prod_p \Gamma(\Delta_p)(1 - F_{1,p}), \tag{4.43}$$

where $\prod_p$ is the probability of finding an electron at a particular quasi-level, $\Gamma(\Delta_p)$ is the tunnelling probability for that particular electron with an energy Δ_p above the ground state and the factor $(1 - F_{1,p})$ is the Fermi-Dirac probability of finding an empty conduction band state.

The emission rate of charge carriers trapped in a potential well by means of phonon-assisted tunnelling may also be described by a different model which was proposed by Ganichev in 1999. [38] In this model the emission rate is defined in terms of the tunnelling time at a given electric field as:

$$e(F) = e(0)exp(\frac{\tau_2^3 q^2 F^2}{3m^*\hbar}). \tag{4.44}$$

With the tunnelling time for a free electron defined as:

$$\tau_2 = \frac{\hbar}{2k_B T} \pm \tau_1, \tag{4.45}$$

where the minus and plus sign corresponds to the weak and strong electron-phonon coupling respectively, and τ_1 the tunnelling time for a bound electron. A comparison between the two models discussed for phonon-assisted tunnelling shows that the model described by Equation 4.44 gives a functional relationship between the emission rate and the electric field strength, and can be used to determine if enhanced emission is due to phonon-assisted tunnelling.

Chapter 5

Characterisation Techniques

5.1 Introduction

This chapter gives a short discussion of the electrical characterisation techniques used in this study. Although the main focus will be on deep-level transient spectroscopy, short descriptions of the current-voltage and capacitance-voltage characterisation are also given, as these were used to confirm the suitability of the diodes for deep-level transient spectroscopy measurements.

5.2 Current-Voltage Characterisation

Previously the current transport mechanisms for metal-semiconductor contacts were described. From Equation 3.19 it follows that the current-voltage characteristics for moderately doped semiconductors in the forward direction is given by: [4]

$$J = J_s \exp[\frac{q(\Delta\phi + V_D)}{k_B T}] \quad \text{for} \quad V_D >> \frac{k_B T}{q}, \tag{5.1}$$

with $\Delta\phi$ the Schottky barrier lowering and J_s the saturation current density, which can be expressed as:

$$J_s = A^* T^2 \exp(\frac{-q\phi_B}{k_B T}). \tag{5.2}$$

Since both the Richardson constant and the Schottky barrier lowering are functions of the applied bias, it then follows that the current-voltage characteristics can be approximately given by the following equation:

$$J = J_s \exp \frac{qV_D}{nk_B T} \quad \text{for} \quad V_D >> \frac{k_B T}{q} \tag{5.3}$$

where n is the ideality factor, and is defined as:

$$\begin{aligned} n &= \frac{q}{k_B T} \frac{\partial V_D}{\partial(\ln J} \\ &= [1 + \frac{\partial \Delta\phi}{\partial V} + \frac{k_B T}{q} \frac{\partial(\ln A^*)}{\partial V_D}]. \end{aligned} \tag{5.4}$$

The Schottky barrier height is given by:

$$\phi_B = \frac{k_B T}{q} \ln(\frac{A^* T^2}{J}) \tag{5.5}$$

From Equation 5.1, it follows that a logarithmic plot of the current versus the applied bias should be linear. In practice, for a good diode, this is valid for a large applied bias until the effects of series resistance become significant. The saturation current density is equal to the extrapolated value of current density at zero applied bias. The ideality factor of the diode may be determined from the slope of the graph while the barrier height may be determined from the extrapolated value of zero current density.

For a diode to be suitable for deep-level transient spectroscopy it is required that its reverse leakage conductance should be negligible compared to its admittance and its series resistance negligible compared to its impedance. In practice a factor ten is more than sufficient. A typical diode with a capacitance of 20 pF has an impedance of roughly 10 kΩ at 1 MHz. Therefore, to be suitable for deep-level transient spectroscopy, the series resistance of the diode should be 1 kΩ or less and its leakage current at 1 V reverse bias should be 10^{-5} A or less.

5.3 Capacitance-Voltage Characterisation

Electric fields exerts a force on the free charge carriers within the semiconductor, resulting in a net flow of charge carriers through the semiconductor which constitutes an electric current. The concentration of these free charge carriers can be obtained through a capacitance measurement as a function of the applied bias (capacitance-voltage measurement). In Chapter 3 we derived an expression for the capacitance of a Schottky diode as a function of applied bias. Rearrangement of Equation 3.15 leads to:

$$\frac{1}{C^2} = -\frac{2}{q\epsilon_s N_D} V_D + \frac{2(V_0 - \frac{k_B T}{q})}{q\epsilon_s N_D}. \tag{5.6}$$

Now, taking the derivative of Equation 5.6 in terms of the applied bias:

$$\frac{d}{dV_D}\frac{1}{C^2} = -\frac{2}{q\epsilon_s N_D}. \tag{5.7}$$

If we assume that the doping concentration is constant throughout the depletion region, then a straight line should be obtained by plotting the inverse squared of the capacitance versus the applied bias. Furthermore, the built-in potential may be determined from the extrapolated value of the applied bias at zero capacitance, while the concentration of these free charge carriers may be determined from the gradient of the graph. If the doping concentration is not constant, then the differential capacitance method can be used to determine the free charge carrier concentration. [4] [39]

5.4 Deep-level Transient Spectroscopy

Deep-level transient spectroscopy (DLTS) is s a widely used and powerful technique to determine many of the parameters related to defects, such as the activation energy, defect concentration and capture cross-section. Deep-level transient spectroscopy is a high frequency thermal scanning technique originally introduced by D.V. Lang in 1974. [40] However, recently a new approach to the analysis of the transient was

developed and is now known as the Laplace-transform deep-level transient spectroscopy. This technique has greatly improved the resolution of capacitance based defect characterisation. [41]

Deep-level transient spectroscopy works by applying a reverse bias to a Schottky diode, in order to establish a depletion region. A filling pulse is then applied, reducing the width of the depletion region, and the traps between the old and new position of the depletion region edges are filled. After the end of the filling pulse, the diode is returned to the quiescent reverse bias and capacitance transient due to the emission of charge carriers from these traps is measured. An illustration of how the capacitance transient is generated, which in turn is used for the deep-level transient spectroscopy, is shown in Figure 5.1. This transient is usually an exponential time dependent transient. In the following sections the principles of this technique will be discussed in more detail. Later in the chapter, the use of deep-level transient spectroscopy to extract various defect parameters will be discussed.

5.4.1 Capacitance Transient

In Section 3.2.2, the equation to determine the depletion region width as well as the capacitance of a Schottky diode was formulated, which will play an important role in describing deep-level transient spectroscopy. For clarity this equation is given again:

$$\begin{aligned} C &= \frac{|\partial Q|}{\partial V_0} \\ &= \sqrt{\frac{q\epsilon_s N_D}{2(V_0 - V_D - \frac{k_B T}{q})}} \\ &= \frac{\epsilon_s}{W}, \end{aligned} \tag{5.8}$$

showing that the capacitance per unit area of the diode depends on the depletion region width, which in turn depends on the applied bias and the charge within the depletion region.

Consider a junction formed between a metal and an n-type semiconductor material in thermal equilibrium. When in thermal equilibrium there is no net flow of electrons between the two materials and the density of free charge carriers within the depletion region negligible, the only charge present is due to the ionised donors. In Figure 5.1 the bulk of the semiconductor containing free charge carriers is indicated by the shaded area, with the depletion region the unshaded area. Now consider the case where there is a defect level E_T that can trap electrons. The filled and empty circles indicate occupied and unoccupied traps respectively. For simplicity, it is assumed that all the traps within the depletion region are empty, while the traps within the bulk of the semiconductor are filled.

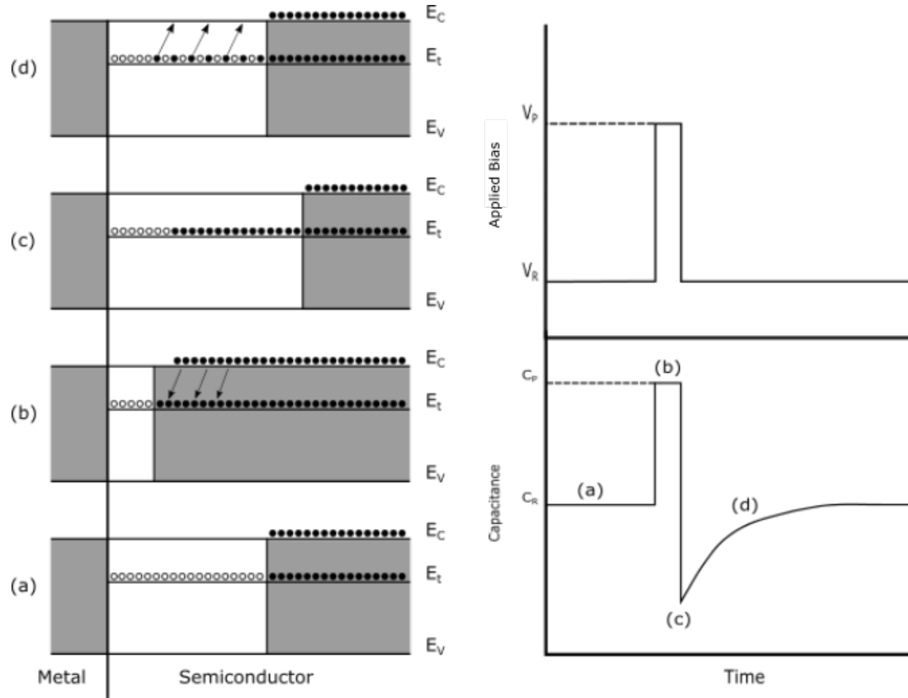

FIGURE 5.1: DLTS principle of operation, and transient formation.

Initially the diode is placed under a quiescent reverse bias, causing the depletion region width to increase and the capacitance to decrease. Traps within the depletion region are now empty and above the Fermi level. A filling pulse (majority carrier pulse) is used to reduce the reverse bias, thus reducing the width of the depletion region and increases the capacitance of the diode. These empty traps are no longer within the depletion region and are able to capture the free electrons. The rate at which these traps are filled can be derived from Equation 4.21, and is given by:

$$\frac{dn_T}{dt} = c_n(N_T - n_T). \tag{5.9}$$

After the filling pulse, the reverse bias is returned, which results in the depletion region width to increase leaving some electrons trapped by traps in the depletion region. Because of this, some of the positive charge density is now compensated by the trapped electrons with an overall decrease of charge density in the depletion region. Therefore a slightly wider depletion region and a slightly lower capacitance will be observed. The traps above the Fermi level filled with electrons will emit electrons to the conduction band by means of thermal processes, if sufficient thermal energy is present. This causes the charge density in the depletion region to increase and the depletion region width to decrease, increasing the capacitance. From Equation 4.21 the rate at which these electrons are emitted is:

$$\frac{dn_T}{dt} = -e_n n_T. \tag{5.10}$$

Integration leads to the exponential decay of the filled traps with respect to time as:

$$\begin{aligned} n_T &= N_T \text{exp}(-e_n t) \\ &= N_T \text{exp}(-\frac{t}{\tau}), \end{aligned} \tag{5.11}$$

with

$$\tau = \frac{1}{e_n}, \tag{5.12}$$

where τ is the emission time constant. Here the assumption is made that the concentration of filled traps is much less than the doping concentration, so that the emission of charge carriers from traps in the depletion region will not alter the width significantly, then it is reasonable to assume that the emission of carriers from the depletion region be described by an exponential decay. The capacitance can then also be described by an exponential decay as:

$$C(t) = C_\infty - \Delta C \text{exp}(-\lambda t), \tag{5.13}$$

with λ the decay rate, and C_∞ the steady-state capacitance. This is true since the capacitance depends on the charge density within the depletion region. By a series expansion of Equation 5.8 the capacitance can be expressed as:

$$C(t) = C_0 - C_0 \frac{n_T}{2N_D}, \tag{5.14}$$

where C_0 the steady-state capacitance at reverse bias V_R. Finally, the capacitance can be rewritten in terms of an exponential decay function:

$$C(t) = C_0 - C_0 \frac{N_T}{2N_D} \text{exp}(-\frac{t}{\tau}). \tag{5.15}$$

This shows that the change in capacitance, due to a pulsing bias, can be used to determine the concentration as well as the emission rates. [42]

5.4.2 Conventional DLTS (C-DLTS)

In order to analyse the data, the emission time constant of the decay has to be determined. The conventional technique uses a double boxcar averager to define a rate window. The double boxcar method works by measuring the capacitance at two separate times, say t_1 and t_2. [40] The difference between these two values is then known as the signal. Thus the signal is given by:

$$S(T) = C(t_1) - C(t_2). \tag{5.16}$$

As the temperature of the sample is scanned, the emission rate changes and the difference in capacitance forms a bell-shaped curve, as is illustrated in Figure 5.2. Initially, at high temperatures, the transient decays very fast, before the first gate, resulting in both gates measuring almost the same capacitance, resulting in a small signal, see top graph in Figure 5.2. As the temperature is lowered the transient decays slower and the signal increases, this process continues up to a point where the first gate measures the capacitance approximately at the bottom of the transient and gate two measures the capacitance approximately at the top of the transient leading

to a maximum in the signal, see middle graph in Figure 5.2. From this point on the transient decays slower and the difference in capacitance measured at the two gates becomes smaller, leading to a smaller signal. Eventually, at much lower temperatures, the decay of the transient is so slow that there is almost no difference in the capacitance as measured by the two gates, therefore the signal returns to zero, see bottom graph of Figure 5.2. This process can be mathematically described by:

$$S(T) = \frac{N_T}{2N_D}(\exp{(-\frac{t_1}{\tau})} - \exp{(-\frac{t_2}{\tau})}). \tag{5.17}$$

As mentioned, there is a temperature for which the signal is a maximum. The time constant where this happens may be obtained by differentiating Equation 5.17 with respect to temperature and solving for the time constant:

$$\tau_{max} = \frac{t_1 - t_2}{\ln t_1 - \ln t_2}. \tag{5.18}$$

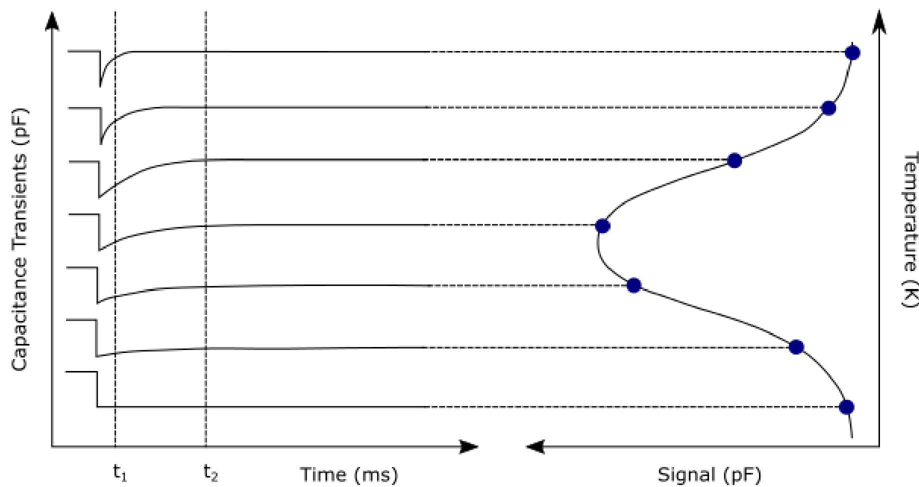

FIGURE 5.2: Illustrates how the conventional DLTS spectra are formed from the capacitance transient changes as a function of temperature. [43]

By using Equations 5.17 and 5.18 the maximum of the signal can be obtained, from which it is clear that the signal is proportional to the trap concentration and the peak height is dependent on the ratio between the times chosen, rather than the their absolute values. [42]

5.4.3 Laplace DLTS (L-DLTS)

The conventional technique described previously has excellent sensitivity, however the resolution of the emission rate and time constant is very poor for studying closely spaced transients. Over the last few years much effort had been done to improve the resolution of this method, but this improvement of resolution came at the expense of noise performance. [44] Thus a new technique with excellent resolution and equally good sensitivity had to be developed.

In 1994, Dobaczewski introduced an improved technique, which measures the transient at a fixed temperature and utilises the numerical inverse Laplace transform to analyse the transients, unlike the conventional method which measures the transient as a function of temperature and utilises the conventional double boxcar analysis. [45] As a result this technique, now known as Laplace deep-level transient spectroscopy (L-DLTS), has an improved resolution by an order of magnitude. Thus this technique is able to separate closely spaced transients typically with time constants differing by a factor two or less, thereby overcoming the major shortcomings of the conventional technique. However this technique is extremely sensitive to noise, therefore the average of a large number of transients is taken to increase the signal to noise ratio.

For a quantitative description of non-exponential behaviour in the capacitance transients, it is assumed that the recorded transients $f(t)$ are characterised by a spectrum of emission rates

$$f(t) = \int_0^\infty F(s) \exp{(-st)} ds \tag{5.19}$$

where $F(s)$ is the spectral density function. To determine a real spectrum of emission rates in the transient, an inverse Laplace transform for the function $f(t)$ should be performed, producing a single or multiple peaks as a function of s. The accuracy of this technique is highly dependent on the signal to noise ratio of the transient, and may be influenced by many factors such as the number of transients averaged, the quality of the sample and other external factors. Laplace DLTS gives an intensity output as a function of emission rate, with the area under each peak directly proportional to the defect concentration.

5.5 Emission Activation Energy

Both techniques described in the previous section can be used to determine the emission rate in order to calculate the activation energy. Using the conventional method requires multiple scans over a large temperature range while varying the rate window. By using Equation 5.17 and 5.18 it can be shown that there exists a maximum peak height for each rate window, which in turn corresponds to a specific temperature. Thus by repeated scans over the specified temperature range while varying the rate window, a maximum peak height corresponding to a specific temperature for each scan is obtained, as shown in Figure 5.3. By using Equation 5.15 the emission rate for each peak corresponding to a specific temperature can be calculated. In Equation 4.16 it was shown that the emission rate may be expressed as:

$$\begin{aligned} e_n &= \sigma_n v_{th,n} N_C \exp(-\frac{E_C - E_T}{k_B T}) \\ &= \frac{2}{\pi^2 \hbar^3} \frac{\sigma_n m_e^* k_B^2 T^2}{g} \exp(-\frac{E_C - E_T}{k_B T}). \end{aligned} \tag{5.20}$$

Taking the logarithm on both sides:

$$\ln \frac{e_n}{T^2} = -\frac{E_C - E_T}{k_B} \frac{1}{T} + \ln \frac{2}{\pi^2 \hbar^3} \frac{\sigma_n m_e^* k_B^2}{g}. \tag{5.21}$$

Assuming that the capture cross-section is independent of temperature, the follows that the emission rate with corresponding temperature can now be used in a logarithmic graph to obtain a linear plot, as seen in Figure 5.4. The gradient of the straight line can be used to calculate the activation energy and the apparent capture cross-section from the intercept with the vertical axis.

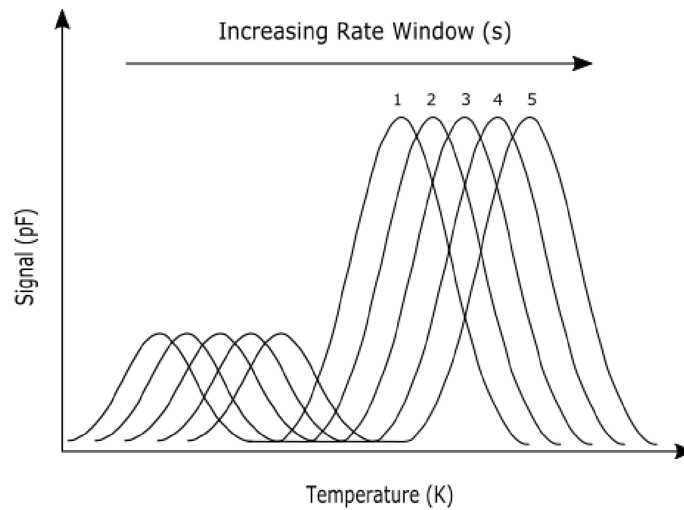

FIGURE 5.3: DLTS signals for different rate window conditions.

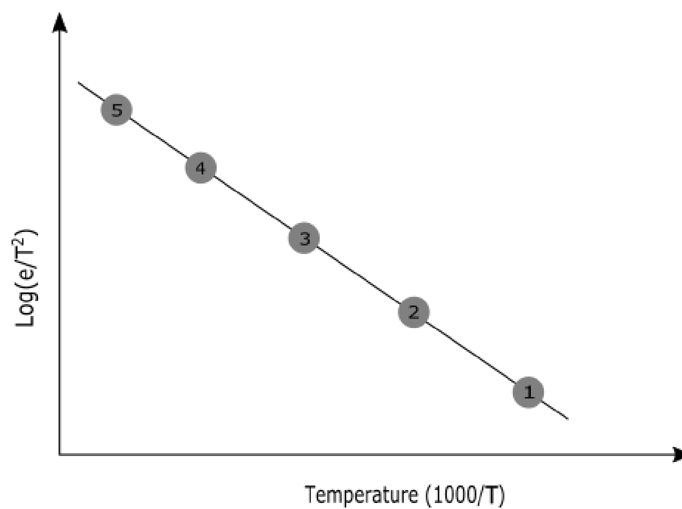

FIGURE 5.4: Arrhenius plot obtained from DLTS signal maxima.

The Laplace method can also be used to determine the activation energy, in a similar fashion to the conventional method. The difference being that emission rates are obtained as a function of temperature. During this method an isothermal scan is done at specified temperatures, in which the emission rate is obtained at that temperature. Thus the emission rates and corresponding temperatures are plotted in the same way as with the conventional method. The Laplace method is used instead of the conventional method since it is able to identify and separate traps with closely-spaced emission rates.

5.6 Defect Depth Profiling

The signal obtained from deep-level transient spectroscopy is directly proportional to the concentration of deep-level defects, which means that the concentration of these defects can directly be obtained from the capacitance change. This change in capacitance can be obtained by completely filling these defects with charge carriers by applying the largest possible filling pulse. The concentration of these filled defects is related to the capacitance by the following equation:

$$C(t) = C_0 - C_0 \frac{n_T}{2N_D}. \tag{5.22}$$

Now, if it is assumed that the filling pulse is large and long enough for all these defects to be completely filled, such that the concentration of filled defects is equal to the total concentration of defects, then Equation 5.22 can be reduced to:

$$N_T = \frac{2\Delta C}{C_0} N_D, \tag{5.23}$$

where ΔC is the change in capacitance directly after the filling pulse and C_0 is the capacitance under the quiescent reverse bias. However, this approach is overly simplistic, especially for low biases and deep defects, and may lead to some serious errors in determining the concentration of these defects. [46]

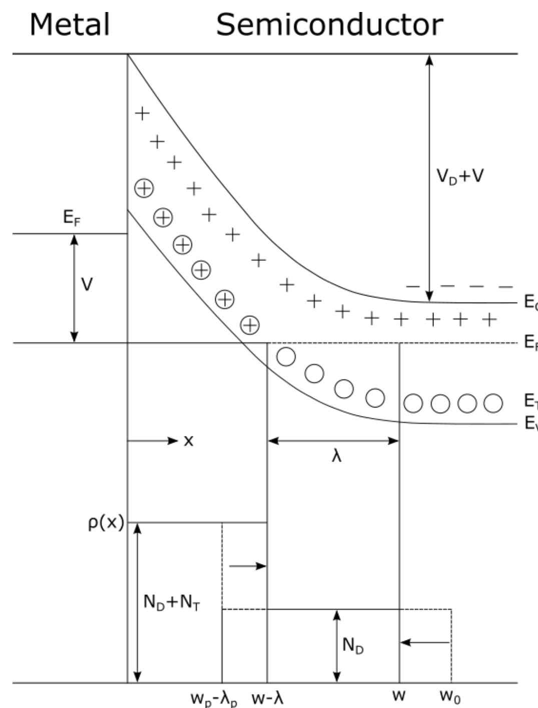

FIGURE 5.5: The energy band diagram and charge density as a function of depth for Schottky diode. The solid line corresponding to the charge distribution under a quiescent reverse bias and the dashed lines is the charge distribution right after the filling pulse which relaxes back to solid line. [47]

A more accurate equation is obtained by taking into account a distance λ shallower than the depletion region edge remaining below the Fermi level, as shown in Figure

5.5. These defects within the region a distance λ from the depletion region edge are filled and do not contribute any change to the capacitance when a filling pulse is applied. [47]

The distance that these deep-level defects cross the Fermi level is denoted by λ, and can be calculated as follows:

$$\lambda = \sqrt{\frac{2\epsilon_s(E_F - E_T)}{q^2 N_D}}. \tag{5.24}$$

To profile the distribution of deep-level defects, the region being profiled needs to be filled with charge carriers. The technique uses a quiescent reverse bias and a variable filling pulse, which is also known as the fixed bias–variable pulse method. [48] This is done by superimposing a forward bias on a quiescent reverse bias during the filling pulse, reducing the resultant reverse bias and hence the depletion region width. Thus increasing the forward bias in multiple steps increases the resultant filling pulse accordingly, this in turn causes the depletion region width to decrease in each step, letting more defects being filled by charge carriers and consequently increasing the peak height. In Figure 5.5 the signal as a function of the filling pulse is shown, where peak height increases with increased applied forward bias.

Directly after applying the filling pulse, the region $w_p - \lambda_p \leq x \leq w - \lambda$ as shown in Figure 5.5, is now able to be filled with charge carriers. Here the subscript p indicates the values of the quantities during the pulse bias. By double integration of Poison's equation across the depletion region during quiescent reverse bias, it follows that the sum of the built-in potential and quiescent reverse bias is equal to:

$$V + V_D = \int_0^{w-\lambda} N_T(x) \cdot x dx + \int_0^{w} N_D(x) \cdot x dx. \tag{5.25}$$

In a similar fashion, the sum of the built-in potential and quiescent reverse bias during the filling pulse is now equal to:

$$V + V_D = \int_0^{w_p-\lambda_p} N_T(x) \cdot x dx + \int_0^{w_0} N_D(x) \cdot x dx. \tag{5.26}$$

By equating these two equations then we are left with:

$$\int_w^{w_0} N_T(x) \cdot x dx = \int_{w_p-\lambda_p}^{w-\lambda} N_D(x) \cdot x dx. \tag{5.27}$$

Assuming that the change in capacitance is small in comparison to the quiescent reverse bias capacitance, and $N_D(x)$ slowly changes in the range $w \leq x \leq w_0$ and $N_T(x)$ slowly changes in the range $w_p - \lambda_p \leq x \leq w - \lambda$, it follows that:

$$\frac{N_T(w_m - \lambda_m)}{N_D(w)} = \frac{1}{(\frac{w-\lambda}{w})^2 - (\frac{w_p-\lambda_p}{w})^2}, \tag{5.28}$$

with:

$$w_m - \lambda_m = \frac{1}{2}[(w - \lambda) - (w_p - \lambda_p)], \tag{5.29}$$

which is the corrected equation to calculate the concentration of deep-level defects.

If λ is small, i.e. the distance the defects cross the Fermi level of the semiconductor is close to the depletion region width, then Equation 5.28 reduces to Equation 5.22. [47]

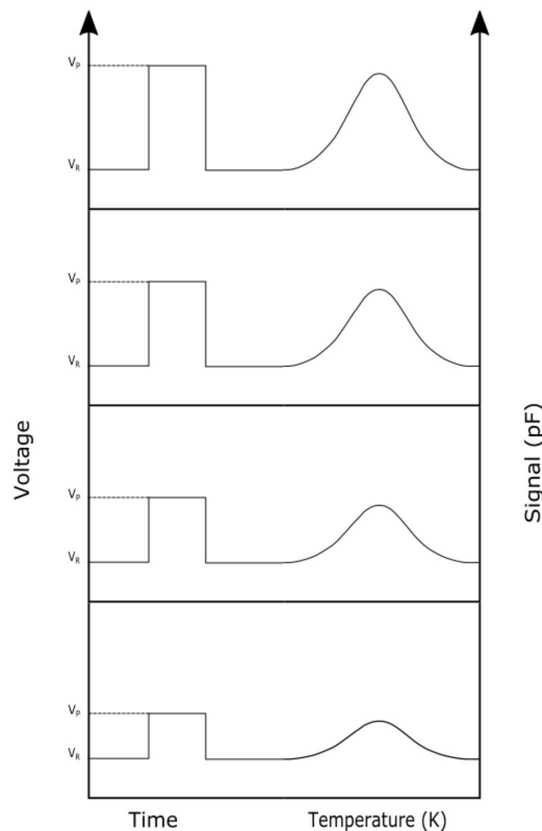

FIGURE 5.6: DLTS signals obtained during depth profiling. On the left we have the filling pulse applied to the Schottky diode, with the bottom being the smallest filling pulse and the top the largest filling pulse. On the left is the corresponding signals obtained through DLTS and L-DLTS measurments. DLTS

It should be mentioned that a linear or non-linear relationship between the depletion region being filled and the signal will be observed for Schottky diodes, depending on whether the defect concentration is uniform or non-uniform. The resolution may be increased by reducing the filling pulse for each step, thus increasing the total number of steps, however this is limited by the Debeye length.

Chapter 6

Experimental Techniques

6.1 Introduction

In this chapter we start by describing the process used to clean the surface of the silicon before contact deposition and how the contacts are formed. Afterwards the radiation source and process for irradiation used will be discussed. Finally the apparatus and system setup for measuring the sample will be discussed.

6.2 Sample Preparation

As mentioned in the first chapter the silicon wafer may be produced using various techniques. But before any Schottky or Ohmic contact can be formed, the silicon wafer should be cut into smaller workable pieces, after which the pieces are cleaned. These pieces shall now be referred to as the samples. The cleaning process can be divided into two steps, first the degreasing of the sample and then etching of the sample. The degreasing process is used to remove any organic contamination from the surface, and the etching process is used to remove any oxide layer from the surface of the silicon.

6.2.1 Cleaning Procedure

The degreasing process consists of washing in three different chemicals namely trichloroethelyne, isopropanol and methanol. For the etching process only hydrofluoric acid were used. The cleaning process is as follows:

1. For degreasing, the sample was placed in a beaker containing the respective chemical, in a quantity just enough to cover the surface of the sample. The beaker was then placed in an ultrasonic bath for five minutes at room temperature, and then rinsed with de-ionised water.

2. After the degreasing process the sample was dipped in a Teflon beaker containing hydrofluoric acid (40%) for approximately twenty seconds after which the sample was removed. This process is used to remove the native silicon dioxide from the surface of the sample. Note that the sample should not be left in the acid for longer than a minute, as pitting may occur.

3. After the twenty seconds in the hydrofluoric acid the sample is dipped in de-ionised water and then blown dry using high purity nitrogen gas in the fume hood, to remove any excess hydrofluoric acid.

6.2.2 Contact Formation

Resistive thermal evaporation is one of the most commonly used techniques for metal deposition. The system consists of the components shown in Figure 6.1. In this technique, the crucible containing the metal to be deposited is heated by a large current flowing through it, thus heating the metal (which in the case of ohmic contacts would be AuSb) indirectly to a high enough temperature to undergo evaporation. The metal vapour is now deposited onto the sample above the crucible, where the rate of deposition is controlled by adjusting the current through the crucible. This technique is only used for metals with low enough melting points such aluminium, gold, lead and nickel and cannot be used to deposit higher melting point metals.

When a material undergoes evaporation it will experience collisions with remaining gas molecules inside the chamber resulting in a fraction of the material being lost, or contamination to occur. Hence one of the requirements for resistive thermal evaporation is a good vacuum during deposition. At room temperature the mean free path at pressures between $10^{-4} - 10^{-6}$ mbar is approximately $45 - 4500$ cm, with the distance between the crucible and the mounted sample at approximately 30 cm. Therefore pressures of at least 10^{-4} mbar or lower is needed for deposition.

Immediately after the cleaning process the sample was placed in the evaporation chamber for Ohmic contact formation, as shown in Figure 6.1. This was done by resistively evaporating 100 nm of AuSb (0.6% Sb) at a rate of 0.1 nm·s^{-1} on the back of the silicon samples. The vacuum was at a level of 10^{-6} mbar to prevent contamination during deposition. Before the Schottky contacts can be made on the front of the sample the cleaning process, as described in the previous section, was repeated.

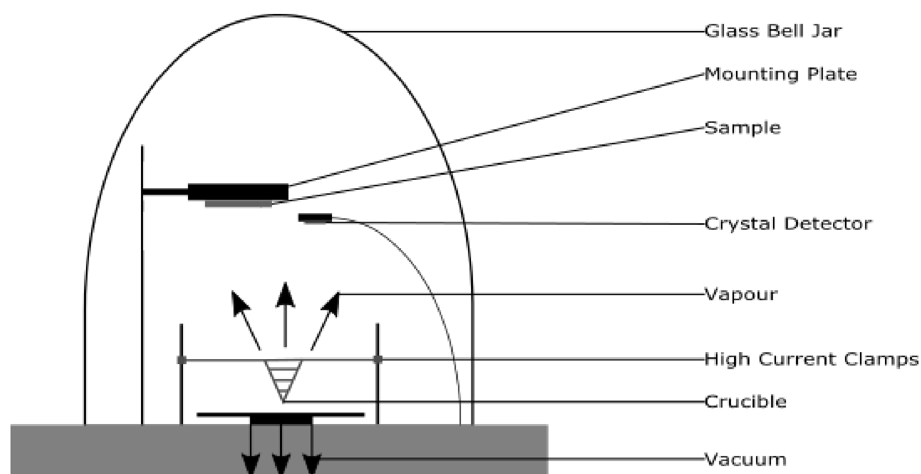

FIGURE 6.1: Schematic diagram of the resistive thermal evaporation system used to deposit the Ohmic and Schottky contacts.

Immediately after the second cleaning process, the sample was placed face down onto a contact mask consisting of circular holes with 0.6 mm diameter, which was in turn mounted in the evaporation chamber. The Schottky contacts were then formed by resistively evaporating 100 nm of pure gold at a rate of 0.1 nm·s^{-1} on the top of the sample. The sample with both ohmic and Schottky contacts is shown in Figure 6.2.

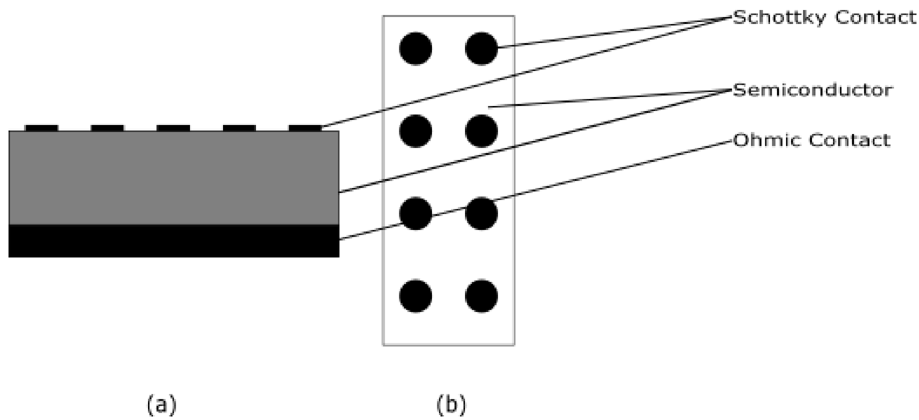

FIGURE 6.2: Schematic diagram showing a sample with both the Schottky and ohmic contacts deposited using resistive thermal evaporation, with (a) the side view and (b) the top view of the sample.

6.3 Sample Irradiation

The defects were introduced by bombarding the sample with high energy alpha-particles in the 5.4 MeV range, from the Schottky side of the sample. The high energy particles were produced by an Americium-241 radiation source. It should be noted that the decay process of Americium-241 consists of multiple decay products each with different energies and fluencies as shown in Figure 6.3.

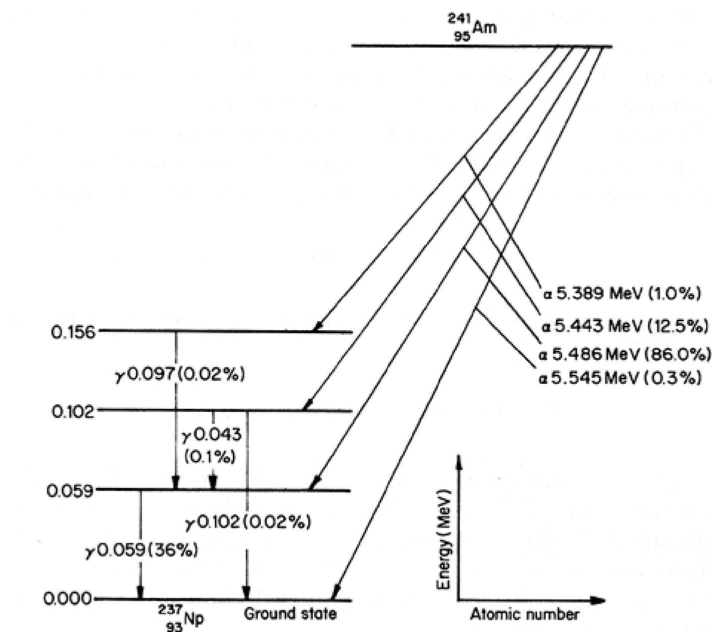

FIGURE 6.3: Shows the decay process of Americium-241 with the respective energies and percentage. [49]

Thus depending on the incident particle type, size, energy and angle some of the particles will be able to penetrate through the sample whereas others may lose all

their energy due to collision and eventually stop within the sample. There exists computer simulation programs that is able to simulate particle irradiation through different materials, with one of these programs known as TRIM simulations. [50] Figure 6.4 depicts the results of the simulation of alpha particle irradiation through a gold-antimony Schottky contact of 100 nm thick into a silicon substrate.

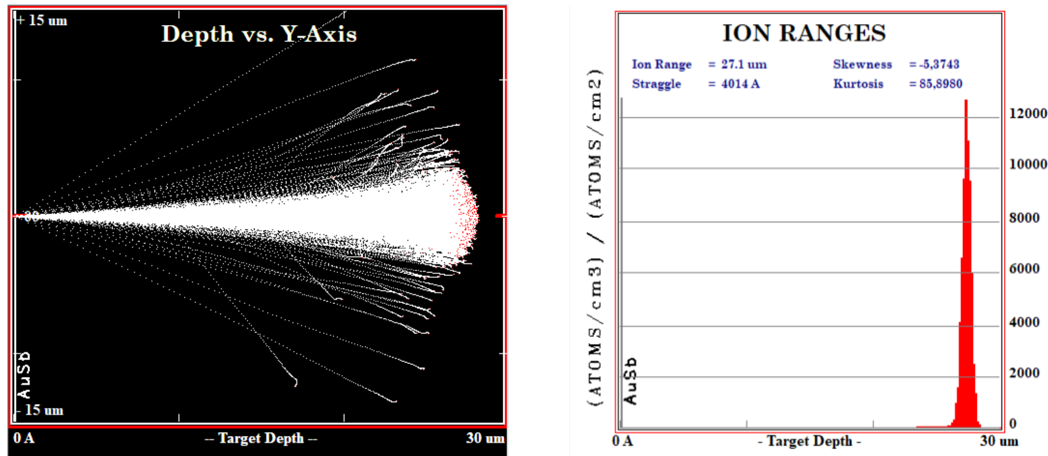

FIGURE 6.4: Shows the TRIM simulation of 100 nm gold-antimony on 200μm of silicon irradiated with alpha particles with 5.4 MeV of energy.

This shows that the alpha particles penetrate up to a depth of 27.1 μm in the silicon substrate. During the deep-level transient spectroscopy measurements will only be observed up to approximately 2 μm beneath the junction. There might be a number of lower-energy particles present and the alpha particles are emitted in random directions. However, given the expected range of 27.1 μm, it is expected that most alpha particles will travel into the silicon significantly deeper than 2 μm. This means the end of range damage will not be observed during measurements, and the damage produced in the observed region should mostly be due to isolated vacancies and interstitials.

6.4 Experimental Setup

With the contacts placed onto the sample, current-voltage and capacitance-voltage measurements were used to determine the quality and electrical properties of the sample. One the samples were confirmed to be of sufficient quality, deep-level transient spectroscopy was then used to characterise the defects in the semiconductor after particle irradiation.

6.4.1 Current-Voltage and Capacitance-Voltage Setup

The electrical properties of a semiconductor that can be determined using current-voltage and capacitance-voltage measurements are the series resistance, free carrier density, barrier height, leakage current and finally the ideality factor. These measurements are important to determine if the contacts formed is adequate for deep-level transient spectroscopy. For deep-level transient spectroscopy the capacitance signal from the sample should have a high signal-to-noise ratio, this corresponds to a high

barrier height, low leakage current and low series resistance. The electrical properties of each sample were measured before each deep-level transient scan, since the contacts tend to degrade after several temperature scans and to monitor the free carrier concentration after irradiation.

Figure 6.3 is a schematic diagram of the system setup used to determine the current-voltage and capacitance-voltage measurements. [51] The current-voltage measurements were measured using an HP4140B pA meter / DC voltage source, whereas the capacitance-voltage measurements were done by an HP4192A LF impedance analyser. The samples were placed inside the probe station which consists of a metal box enclosure to eliminate any light and electrical noise. The personal computer contains the software used to do the measurements and is connected to the current meter and impedance analyser, to store the measured data.

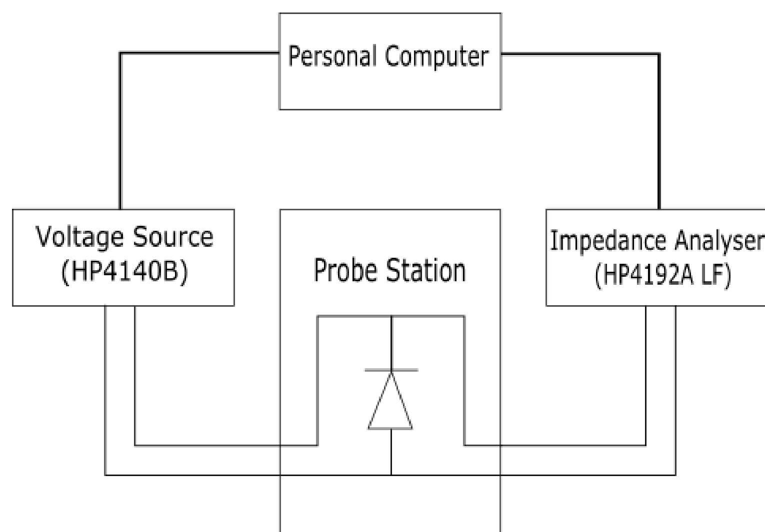

FIGURE 6.5: Schematic diagram showing the system setup used for the current-voltage and capacitance-voltage measurements.

6.4.2 Deep-Level Transient Spectroscopy Setup

Deep-level transient spectroscopy was the primary method used to characterise the defects present in the sample before and after irradiation. The system setup comprised of the following components:

- Cryostat: The sample was mounted inside a cryostat. The cooling is done by using a closed loop helium gas system which can reach temperatures as low as 20 K relatively fast, where an electric heater is used to maintain or increase the temperature.
- Vacuum Pump: The vacuum pump places the inside of the cryostat under a vacuum to thermally insulate the inside of the cryostat from the outside. The vacuum also insures that no condensation is present on inside of the cryostat.
- Temperature Controller: The temperature controller stabilises the temperature of the sample by controlling the current flowing to the heater by means of a

PID loop. In this manner the temperature can be stabilised accurately to the desired temperature.

- Capacitance Meter: The capacitance meter is used to measure the capacitance transients produced by the sample at extremely high speeds and precision.
- Variable Capacitor: The variable capacitor is directly connected to the capacitance meter and is used to reduce the observed capacitance by subtracting a constant capacitance. This allows the capacitance meter to be set to a more sensitive scale than was previously possible.
- Pulse Generator: The pulse generator is used to supply the desired quiescent bias voltages and the filling pulse to the sample, for instances the laplace card can not provide.
- Laplace Card: The Laplace card is placed inside a personal computer and is in turn connected to the pulse generator, capacitance meter and the temperature controller through the IEEE-488-Bus. The Laplace card reads the analogue signal from the capacitance meter and translates it to digital data for processing. [52]

The complete system setup and how they are connected is shown in Figure 6.4. The sample is placed on indium foil, which is then electrically isolated from the system by means of a sapphire disk. The two probes used serve the following functions: firstly connecting the sample electrically to the outside world, secondly to put pressure on the contact to hold it in place and ensure sufficient thermal contact. One of the probes is connected directly to the Schottky contact with the other probe connected to the Ohmic contact through the indium foil.

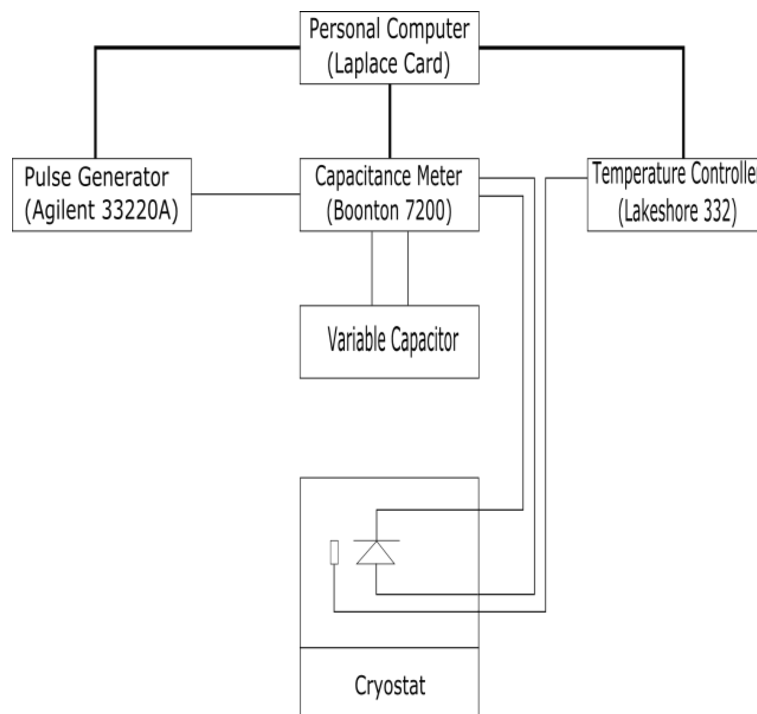

FIGURE 6.6: Schematic diagram showing the system setup used for deep-level transient spectroscopy. [51]

6.4.3 Annealing Setup

Annealing was performed using a closed chamber consisting of an electric heating block, which is able to reach a maximum temperature of 750 K in an extremely short period of time, with a heating rate of 10 K/min with an overshoot of less than 1 K. The electric heating block is connected to a temperature controller that uses a PID control loop to decrease or increase the current to stabilise the temperature within the chamber. The chamber is also connected to a vacuum pump to ensure that no contamination occurs during annealing, as well as to insulate the inside of the chamber from the outside to ensure constant temperature throughout.

Annealing was carried out by opening the chamber and clamping the sample to the heating block and then closing it afterwards. The vacuum pump was then used to create an inert atmosphere before annealing started. When the desired vacuum was reached the heating block was heated to the desired temperature. After annealing, the sample was immediately removed from the annealing chamber and placed into the cryostat for further measurements. [53]

Chapter 7

Results and Discussion

7.1 Introduction

The type of radiation used for irradiation is important as this may lead to different defects that are being introduced. For instance, gamma irradiation consists solely of electromagnetic radiation, hence only point defects will be introduced. With particle irradiation, not only will point defects be introduced but also cluster related defects. The rate at which these cluster related defects are introduced will epend on the mass, charge and energy of the incident particle, where increased rates are observed with heavier, charged particles. Since some clusters are not stable at room temperature, annealing occurs during irradiation. [31] Thus it is important that directly after irradiation the samples are kept cool to avoid further annealing. Alpha particle irradiation was used, and although the end-of-range depth is significantly greater than the depletion region width, some end-of-range damage may be expected in the region probed by DLTS due to the energy spectrum of the particles and their random directions. Thus some cluster related defects will be expected. These results will then be compared to literature and previously obtained results using electron irradiation to highlight differences that might be attributed to end-of-range damage.

In Figure 7.1 is a conventional DLTS spectrum of the sample immediately after irradiation at room temperature. The spectrum displays many of the common radiation-induced defects in silicon. [31] At temperatures below 100 K only one distinct peak could be identified, which corresponds to the superposition of two peaks. The one is a vacancy related defect and is attributed to the $VO_i^{(-/0)}$ defect level, also known as the A-center, with the other peak being the $C_iC_s^{(-/0)}$ defect level. Note that the superposition of the $VO_i^{(-/0)}$ defect level and the $C_iC_s^{(-/0)}$ defect level cannot be resolved by high resolution deep-level transient spectroscopy technique, since both have similar capture cross sections and activation energies. However since they anneal out at different temperatures, they can be distinguished by performing an annealing study. [54] [55]

In the higher temperature range of the DLTS spectrum, two distinct peaks can be identified and are attributed to the two charged states of the divacancy defect, with the first being the $V_2^{(=/-)}$ defect level at round about 125 K and the second being the $V_2^{(-/0)}$ defect level roughly at 225 K, both of which are well known. Due to the phosphorus doping of the silicon samples an additional defect containing vacancies can form when the vacancies combines with the phosphorus atoms to form the $PV^{(-/0)}$ defect level, also known as the E-center. The signal from the $V_2^{(-/0)}$ defect level overlaps with the $PV^{(-/0)}$ defect level which causes the difference in the amplitude of the peak at 125 K compared with that of the peak at 225 K. Since the peaks

are due to two charge states of the same defect equal introduction rate for these two defect levels is expected. This is indeed the case after non-particle irradiation, such as gamma irradiation. However, this is not the case with particle irradiation, such as alpha particle irradiation, where the introduction rates of the $V_2^{(-/0)}$ defect level and the $V_2^{(=/-)}$ defect level are not equal. This will be observed in the annealing curves discussed later in the chapter, where the concentration of the $V_2^{(-/0)}$ defect level will be significantly greater than that of the $V_2^{(=/-)}$ defect level. This is well known as the suppression of the $V_2^{(=/-)}$ defect level associated with the cluster effect. [28]

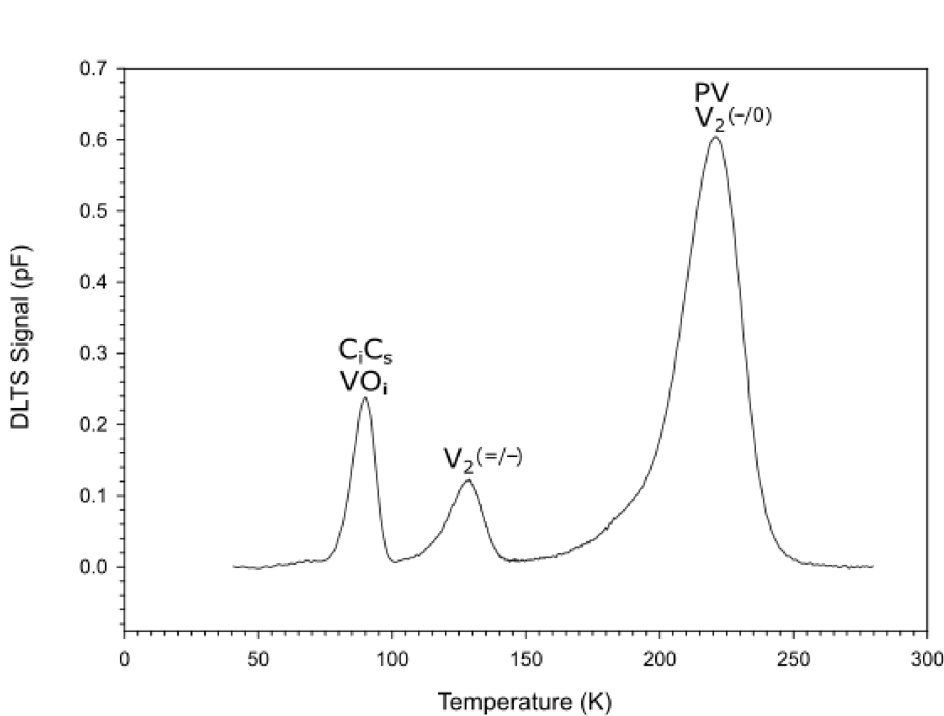

FIGURE 7.1: Conventional deep-level transient spectroscopy spectrum of an n-type silicon Schottky diode after room temperature irradiation with alpha particles. These measurements were recorded at a quiescent reverse bias of V_R = -2 V, with a filling pulse of V_p = 0 V, pulse width of 1 ms and a rate window of 80 s^{-1}.

This clustering effect does not only suppress the peak height at 125 K but also accounts for the broadening of the peak at 225 K, which is due to a change in the local conditions of the defect. The clustering effect is also the sole cause of the shoulder peak at 205 K, which can be separated from the peak at 225 K. With non-particle irradiation and low energy particle irradiation this shoulder peak is not observed. [53] [28]

Listed in Table 7.1 are the peaks observed in this study compared to literature values. A close correlation between the DLTS spectrum in Figure 7.1 and the values listed in mentioned table can be made. From this, it seems that the most prominent defects observed in alpha-particle irradiated silicon correspond to those observed in electron-irradiated silicon. More solid evidence will be presented later in the chapter when their DLTS signatures will be compared. Note that the peak temperature in this study was determined at a rate window of 80 s^{-1}. Some variation in the peak temperature from literature values may be due to literature using a different rate

window. Therefore this provides only a rough comparison.

In the next section, we will use an annealing study to show that there are some differences, and that there is maybe another new unknown defect present.

TABLE 7.1: Comparing the literature values of the radiation-induced defects in silicon after particle irradiation at room temperature with the experimental values obtained during this study.

Defect	Peak Temperature (K)		Annealing Temperature (K)		Reference
	This Study	Literature	This Study	Literature	
$C_i^{(-/0)}$	-	57	-	300	[56], [30]
$C_iC_s^{(-/0)}$ B	65	58	600 - 610	520	[56], [55]
$C_iC_s^{(-/0)}$ A	85 - 90	83	600 - 610	520	[55]
$VO_i^{(-/0)}$	85 - 90	84	620	620	[57], [58]
$V_2^{(=/-)}$	125	119	630	610	[54], [57], [58]
$V_2^{(-/0)}$	210 - 225	202	630	610	[54], [57], [58]
$PV^{(-/0)}$	210 - 225	210	420	460	[59], [60], [61]

7.2 Annealing Profiles

Figure 7.2 shows the DLTS spectra after isochronal annealing of the sample after alpha particle irradiation. During isochronal annealing temperature steps of 10 K for 15 min each were used. Also, each of the conventional spectra is shifted upwards for clarity, with the highest spectrum being the un-annealed sample. Looking at the lower temperature range of the DLTS spectra, the only dominant peak present is the $VO_i^{(-/0)}$ defect level, with a small unknown peak at 70 K. Initially, the concentration of the $VO_i^{(-/0)}$ defect level increased during the first few annealing steps where it reached a maximum after annealing at 440 K. Only at annealing temperatures of above 440 K do we see a significant decrease of the $VO_i^{(-/0)}$ defect level concentration. At 540 K it was almost half of its original concentration, and at temperatures above 620 K it did completely annealed out. [57] [58]

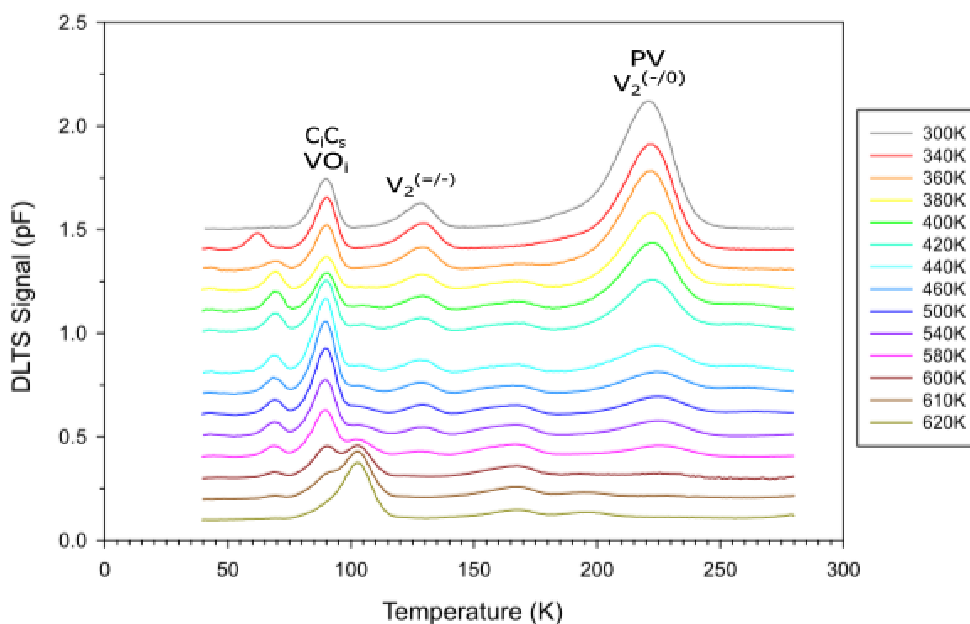

FIGURE 7.2: Conventional deep-level transient spectroscopy spectra of the alpha particle irradiated sample after isochronal annealing consisting of 10 K steps for 15 min each. These measurements were recorded at a quiescent reverse bias of V_R = -2 V, with a filling pulse of V_p = 0 V, pulse width of 1 ms and a rate window of 80 s^{-1}.

It should be mentioned that the cooling conditions (with or without an applied reverse bias) of the sample had a major effect on the level associated with the $C_iC_s^{(-/0)}$ defect level. This is illustrated in Figure 7.2 where the un-annealed sample had no peak present at 70 K, but in the DLTS spectra for the annealed sample a peak could be observed at 70 K. This is due to the fact that the $C_iC_s^{(-/0)}$ defect level at 340 K is known to be a bi-stable defect, and depending on the conditions may be in two different configurations. If the defect is in the negative charged state (occupied by an electron) then configuration A is more stable, while in the neutral charged state configuration B is more stable. Thus by cooling the sample with zero bias such that the defect is in the negative charge state to low temperatures results in configuration

A and no peak will be observed at 70 K, as for the un-annealed sample. By placing the sample under reverse bias such that the defect is in the neutral charge state, then cooling results in configuration B. The energy required for the configuration change at such low temperatures cannot be overcome, hence the defect can now be filled with electrons and the peak at 70 K will be observed. [30]

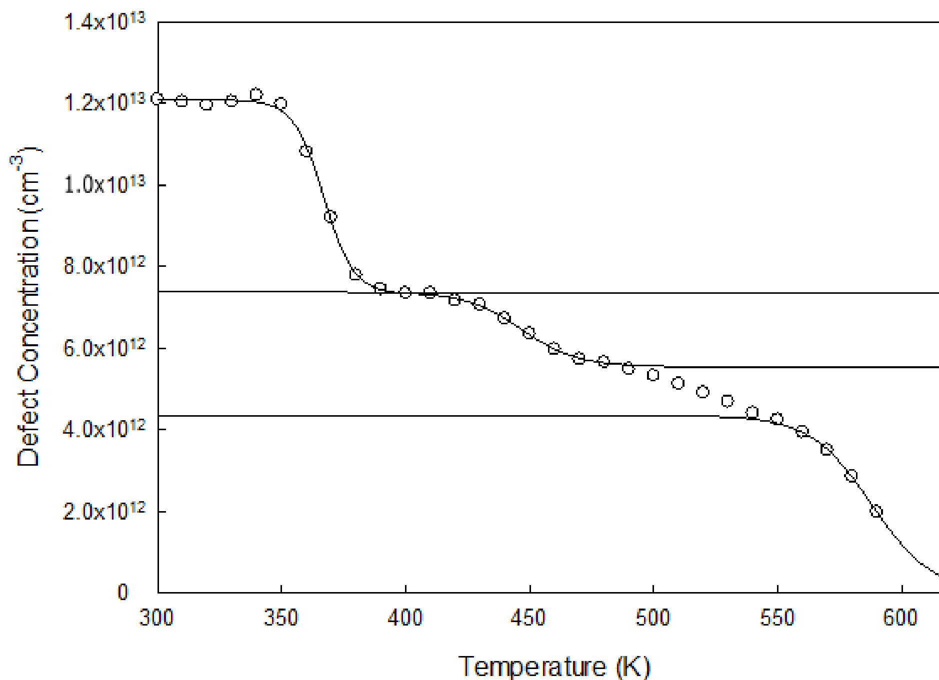

FIGURE 7.3: Isochronal annealing of the peak at 125 K associated with the double negative divacancy directly after alpha particle irradiation measured at a depth of 1 μm. Annealing was done at 10 K steps for 15 min each. The line plots is drawn using a program to show the three distinct annealing processes.

In the middle of the temperature range of the DLTS spectra the only significant peak is due to the $V_2^{(=/-)}$ defect level at 125 K. A small increase of its concentration can be observed during the initial annealing, which can be explained by the relaxation of cluster regions, which release some vacancies of which some combine to form divacancies. [28] With the first few annealing steps no change in concentration was observed, not until annealing temperatures reached 360 K. At this point a noticeable decrease in concentration was observed, which continued up and until 400 K. This annealing is probably not due to the divacancy, but may be due to an unknown defect not previously detected but needs to be investigated further. For clarity, we will refer to this defect as defect X. In Figure 7.3 the isochronal annealing for the peak consisting of the $V_2^{(=/-)}$ defect level is shown. At 420 K another annealing stage can be observed, where the concentration decreases linearly until annealing at 550 K, this corresponds to the annealing of the clusters present in the sample. We will also notice the annealing in the other charge state of the divacancy, providing strong evidence that it is the divacancy annealing out. A possible mechanism might be that the clusters release interstitial defects that combine with the divacancy leading to the formation of single vacancies which quickly diffuse away. Another noticeable decrease in concentration did occur, which corresponds to the $V_2^{(=/-)}$ defect level

being annealed which will be completely removed from the sample at annealing temperatures higher than 610 K. These results agree with other literature as listed in Table 7.1. [62] [63]

After annealing at a temperature of 360 K an unknown peak at approximately 160 K was formed. At higher annealing temperatures the broadening of this unknown peak is observed, which can be explained by the introduction of another unknown closely spaced peak. The concentration of this unknown defect seems to be increasing to maximum at an annealing temperature of 440 K, where it then decreases slowly, but it was still detectable even after annealing at 620 K. Interestingly, the introduction of this peak seems to correspond to the annealing out of the $PV^{(-/0)}$ defect level described in the next paragraph. However, no clear relationship could be established. At annealing temperatures of 580 K another unknown peak can be observed to be formed at 105 K, which increases in concentration beyond the 620 K annealing temperature. Both of these peaks have been reported in literature, but no clear assignment could be made. [28] [63]

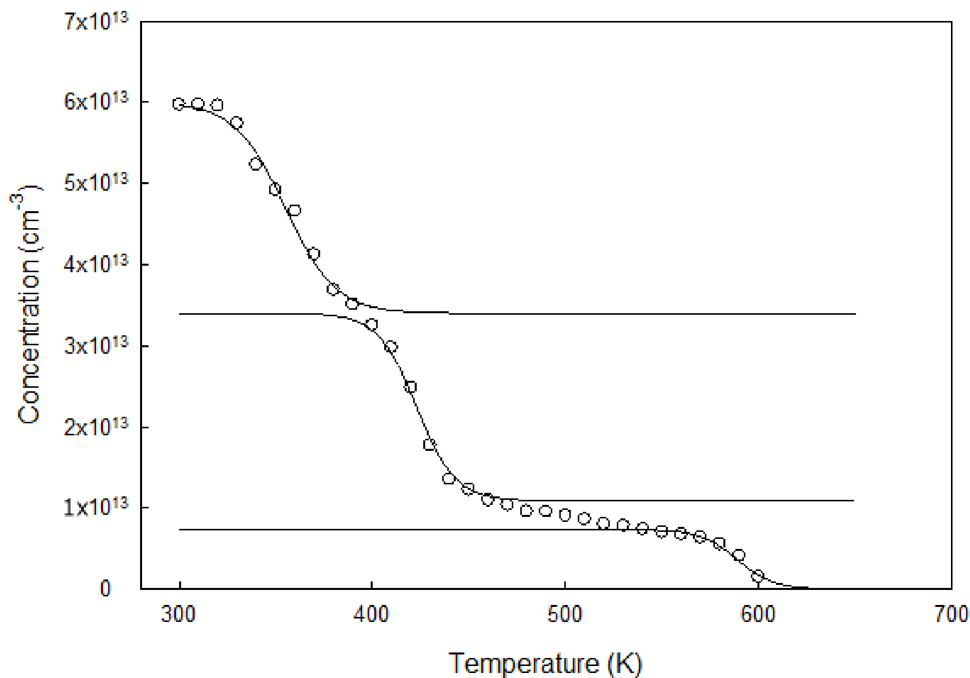

FIGURE 7.4: Isochronal annealing of the single negative divacancy directly after alpha particle irradiation measured at 225 K at a depth of 1 μm. Annealing was done at 10 K steps for 15 min each. The line plots is drawn using a program to show the three distinct annealing processes.

In the higher temperature range there is one peak present throughout the isochronal annealing process, situated at 225 K. As mentioned earlier this peak is due to two defect states, namely the $V_2^{(-/0)}$ defect level and $PV^{(-/0)}$ defect level. [60] In Figure 7.2 it can be seen that as soon as annealing at room temperature starts to about 440 K that there is a sharp decrease in concentration, which corresponds to the annealing of the $PV^{(-/0)}$ defect level. [61] The annealing of the peak is accompanied by the shift of the peak to slightly higher temperatures after annealing; this is in agreement

with the higher emission rate of the $PV^{(-/0)}$ defect level compared to the $V_2^{(-/0)}$ defect level at a given temperature. From this temperature the concentration decreases linearly with annealing temperature to about 550 K, where another sharp decrease in concentration is observed, in this case corresponding to the $V_2^{(-/0)}$ defect level being annealed. [62] Both of these annealing stages correlate with the annealing of the $V_2^{(=/-)}$ defect level, as expected. In Figure 7.4 the isochronal annealing profile for this peak is shown. In the figure we see three stages of annealing instead of the expected two, thus this means that there should be three distinct defects involved. The third defect may correspond to phosphor related defects, possibly the $C_iP_s^{(-/0)}$ defect level. [64] [65]

In summary, comparing the isochronal annealing profiles as shown in Figure 7.3 and 7.4 a few comparisons can be drawn. First, in both spectra three and four annealing stages can be identified. Secondly, a region where the concentration decreases approximately linearly with annealing temperature can be distinguished, where this linear region corresponds to the temperature range of 440 K to approximately 550 K. This region can only be seen in alpha particle irradiation and not in low energy electron irradiation. Therefore, we suggest that this linear region is due to the annealing of cluster related defects. Thirdly, both of these spectra shows the annealing of the divacancy, which occurs around 550 K to about 610 K to be completely removed. Finally, there exists an initial annealing stage between 350 K and 400 K the peak at 125 K, which was not observed in the peak at 225 K and is therefore believed to be due to defect X, only present in alpha particle irradiation.

7.3 Activation Energy and Apparent Capture Cross-Section

In Figure 7.5 the Arrhenius plots for the peaks at 125 K and at 225 K are shown. On the left-hand side the blue line corresponds to the $PV^{(-/0)}$ defect level, whereas the red line corresponds to the $V_2^{(-/0)}$ defect level, as measured by L-DLTS. On the right-hand side of the figure, we have the black line which corresponds to the defect X and the $V_2^{(=/-)}$ defect level combined. Where the green line corresponds to only the $V_2^{(=/-)}$ defect level, with defect X completely removed through annealing.

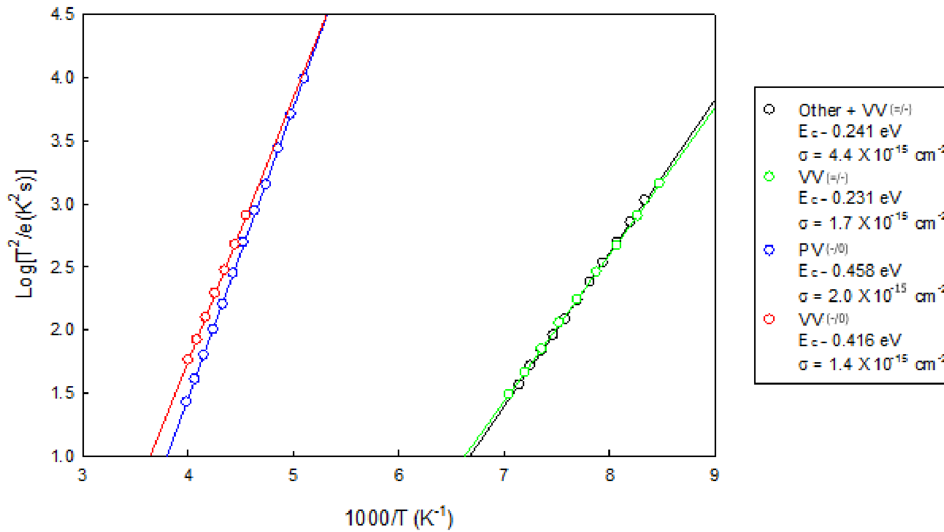

FIGURE 7.5: Arrhenius plot obtained for the single negative divacancy (red) and single negative phosphorous vacancy after annealing and the double negative divacancy before (black) and after (green) annealing.

The activation energy for the $PV^{(-/0)}$ defect level and the $V_2^{(-/0)}$ defect level was found to be 0.458 eV and 0.416 eV respectively. The apparent capture cross-section was found to be approximately 2.0×0^{-15} cm^2 defect level for the $PV^{(-/0)}$ defect level and 1.4 $\times10^{-15}$ cm^2 defect level for the $V_2^{(-/0)}$ defect level. The activation energy for the $V_2^{(=/-)}$ defect level was found to be 0.231 eV with an apparent capture cross-section of about 1.7×10^{-15} cm^2.

In Table 7.2 the literature values of some defects that were introduced during particle irradiation at room temperature are listed, with corresponding electrical properties. When comparing the values obtained in Figure 7.5 with that in Table 7.2 we can see that they correlate with one another. This shows that the peak at 125 K does indeed correspond to the literature value of the $V_2^{(=/-)}$ defect level and the peak at 225 K to the $V_2^{(-/0)}$ defect level and $PV^{(-/0)}$ defect level obtained during the conventional DLTS measurements. By comparing the activation energy and the apparent capture cross-section of the peak at 225 K before and after annealing step at 350 K , it is clear that there is a difference. Where the difference in activation is -0.017 eV and apparent capture cross-section is 2.2×10^{-15} cm^2 which is double the literature value for the $V_2^{(=/-)}$ defect level and can account for the fact that there exists an unknown defect. Due to the overlap of these two peaks, the signature of defect X can not be determined accurately.

TABLE 7.2: Comparing the literature values of the radiation-induced defects in silicon after particle irradiation at room temperature with the experimental values obtained during this study.

Defect	Enthalpy (eV)		Capture Cross Section (cm^2)		Reference
	This Study	Literature	This Study	Literature	
$C_i^{(-/0)}$	-	-0.105	-	6.00×10^{-15}	[30], [56], [66]
$C_iC_s^{(-/0)}$	-	-0.171	-	1.44×10^{-15}	[55]
$VO_i^{(-/0)}$	-	-0.172	-	6.15×10^{-15}	[54], [57], [58]
$V_2^{(=/-)}$	-0.231	-0.224	1.70×10^{-15}	2.20×10^{-15}	[54], [57], [58]
$V_2^{(-/0)}$	-0.416	-0.415	1.40×10^{-15}	1.50×10^{-15}	[54], [57], [58]
$PV^{(-/0)}$	-0.458	-0.456	2.00×10^{-15}	3.70×10^{-15}	[59], [60], [61]

7.4 Introduction Profile

An introduction profile is used to determine the rate at which defects are introduced after irradiation. In order to attain the introduction rate a graph of concentration as a function of time is plotted. In Figure 7.6 the black line corresponds to the concentration of the $V_2^{(=/-)}$ defect level and that of the defect X combined, which corresponds to the peak at 125 K. Where the red line corresponds to the concentration of the $V_2^{(=/-)}$ defect level after annealing at 530 K for one hour. By subtracting these, we obtain the green points, corresponding to the concentration of the defect X. Both the black and the red points could be fitted by a linear fit, however the green dots were fitted better by a parabolic curve as shown. We therefore conclude that the introduction rate of the $V_2^{(=/-)}$ defect level follows the zeroth-order rate, meaning that the concentration increases linearly with time, as can be seen with the red line. [31] On the other hand, the new defect follows the first-order rate, since its concentration is fitted better by a parabolic curve, indicating that defect X is dependent on the concentration of the $V_2^{(=/-)}$ defect level and increases quadratically with time.

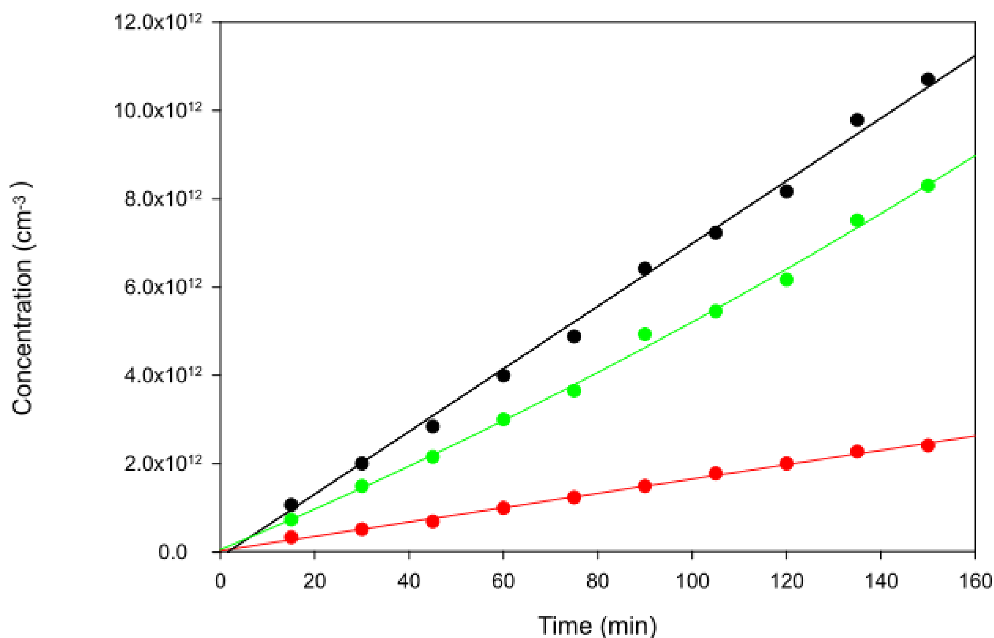

FIGURE 7.6: Defect concentration of the double negative divacancy as function of time directly after alpha particle irradiation (black) and after annealing (red) at 530 K for 60 min.

7.5 Depth Profile

A depth profile is used to determine the concentration of defects at a specific depth below the surface of the semiconductor after irradiation. As discussed in Section 5.6, a depth profile is obtained by plotting the concentration as a function of depth obtained from the DLTS measurements. [53] In Figure 7.7 is such a profile where the concentration of the $V_2^{(=/-)}$ defect level is plotted as a function of depth. In order to investigate the effect of annealing, the sample was irradiated with alpha particles at room temperature, afterwards isochronal annealing in steps of 10 K for 15 min each were done, where a depth profile have been taken in between each step.

In Figure 7.7 only three representative depth profiles are shown. Here the red line represents the depth profile after isochronal annealing at 300 K, which is the concentration of all the defects giving rise to the peak at 125 K present after alpha particle irradiation. The blue line is after isochronal annealing at 400 K, which corresponds to the concentration of the linear region in the annealing profile of the $V_2^{(=/-)}$ defect level, as described previously. Finally, the green line is the isochronal annealing at 550 K, with the concentration of the $V_2^{(=/-)}$ defect level only. This figure shows that there is a significant difference in concentration between annealing, which again, substantiates the fact that there should be another new unknown defect X with the combined concentration being roughly equal to the sum of the concentration of the two defects. It can also be seen that the concentration of the $V_2^{(=/-)}$ defect level and the new unknown defect are constant as a function of depth.

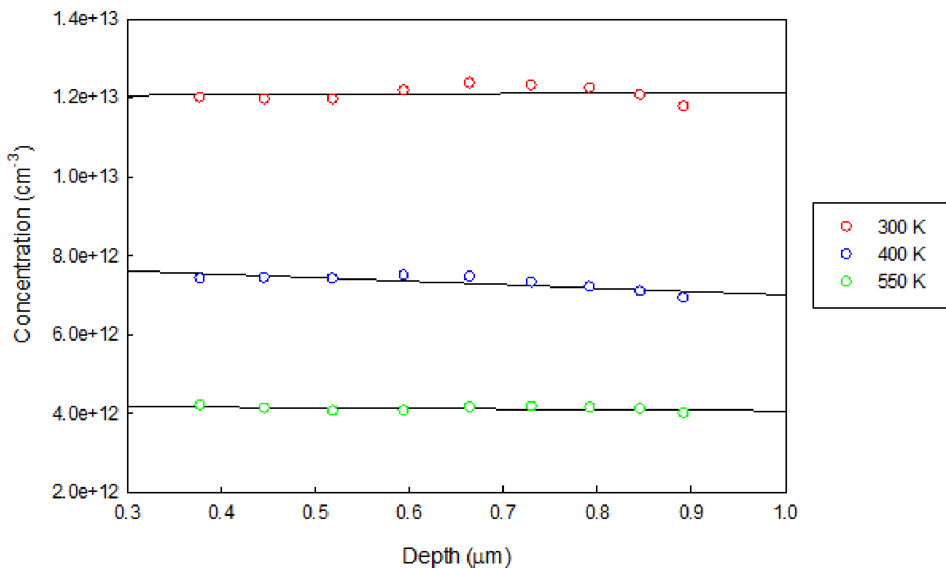

FIGURE 7.7: Depth profile of the double negative divacancy after isochronal annealing at set temperatures.

Again, in Figure 7.8 only three depth profiles for the peak at 225 K are shown. As before, the red line corresponds to the depth profile after isochronal annealing at 300 K, the blue line is after isochronal annealing at 400 K, and the green line corresponds to the isochronal annealing at 550 K. Here the red line represents the concentration of the whole peak after alpha particle irradiation. The blue line is the concentration

of the $PV^{(-/0)}$ defect level, the linear region and the $V_2^{(-/0)}$ defect level. Whereas the green line is only the concentration of the $V_2^{(-/0)}$ defect level. By comparing Figure 7.7 and 7.8 a few observation can be made. It can be assumed that the phosphorous vacancy and both charged states of the divacancy are constant as a function of depth. It can also be seen that the concentration of the $V_2^{(=/-)}$ defect level is almost three times less that the concentration of the $V_2^{(-/0)}$ defect level, this is not a one-to-one relationship as shown by other studies when electrons were used. This discrepancy is due to the suppression of the $V_2^{(=/-)}$ defect level after irradiation with heavier and more energetic particles. [67] [28]

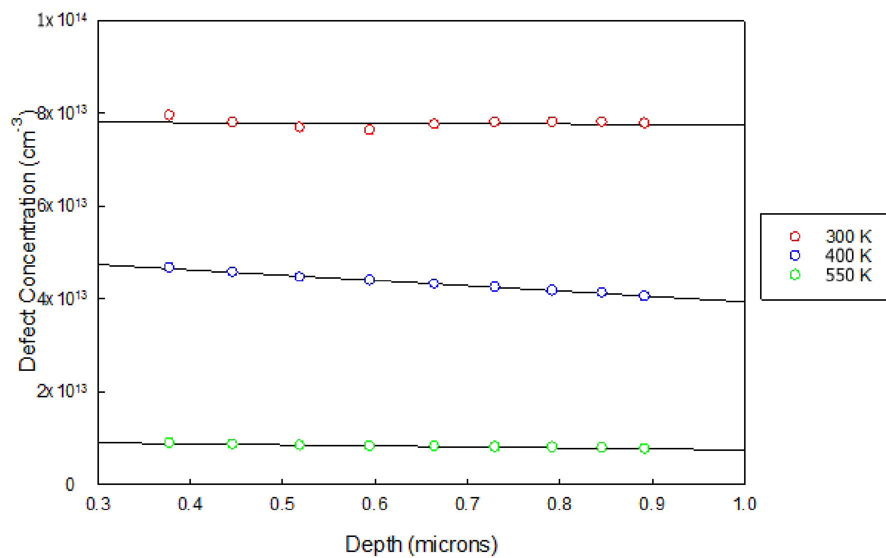

FIGURE 7.8: Depth profile of the single negative divacancy after isochronal annealing at set temperatures.

7.6 Electric Field Effect

As discussed in Section 4.7 the intrinsic electric field is increased by increasing the applied bias, and by doing so, increasing the emission rate of charge carriers through the Poole-Frenkel effect or by means of phonon-assisted tunnelling.

In order to obtain the electric field dependence of the sample after alpha particle irradiation, the sample was annealed at 550 K to remove any other defects, remaining with only the two charged states of the divacancy. In the figures the emission rates were plotted as a function of electric field strength, where the reverse bias was varied from -5 V to -1 V in 0.1 V steps, where both the filling pulses were 0.2 V with a pulse width of 1 ms.

The electric field dependence for the $V_2^{(=/-)}$ defect level is plotted in Figure 7.9, where Figure 7.10 is the electric field dependence for the $V_2^{(-/0)}$ defect level. In both figures the left hand side corresponds to the Poole-Frenkel effect (where the emission rate depends on $E^{1/2}$, and with the right hand side corresponding to phonon-assisted tunnelling (where the emission rate depends on E^2). In both figures we can see that the emission rate does in fact increases with increase in electric field strength, where the gradient for both charged states of the divacancy to be approximately equal. It can also be noted that both charged states have a weak field dependence, since the gradient of the lines is small, and the emission rate increases slowly with in creasing field strength. Finally, by comparing the left with the right hand side for each charged state it can be observed that the emission rate plotted against $E^{1/2}$ resulted in a better linear fit, thus the field enhancement of the emission rate for the divacancy is best described by the Poole-Frenkel effect.

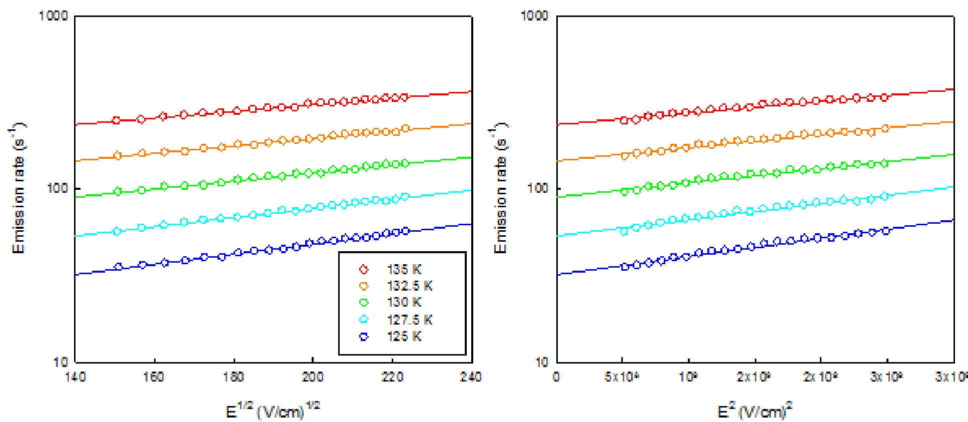

FIGURE 7.9: Electric field dependence of the double negative divacancy after annealing. With the left hand side Poole-Frenkel effect and the right hand side phonon-assisted tunnelling.

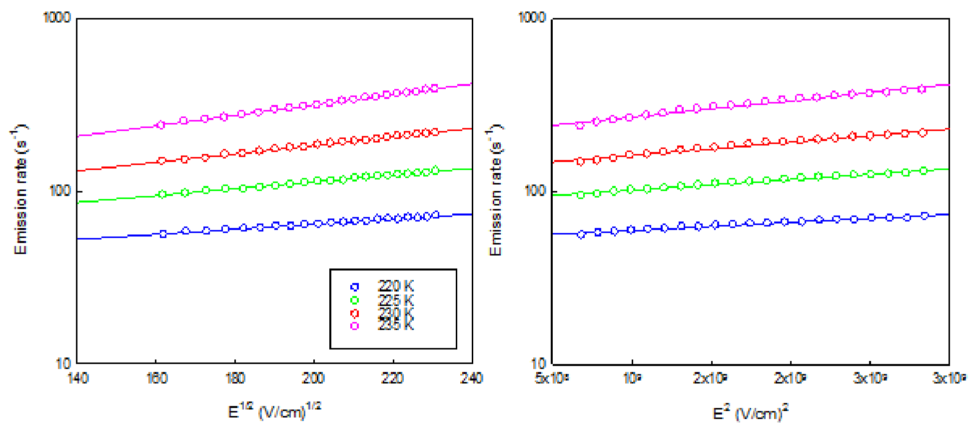

FIGURE 7.10: Electric field dependence of the single negative divacancy after annealing. With the left hand side Poole-Frenkel effect and the right hand side phonon-assisted tunnelling.

Chapter 8

Conclusions

During this research project we set out to investigate the properties of the divacancy in alpha-particle irradiated silicon. By comparison with literature, the common radiation-induced defects were identified. Specifically, the peaks related to the divacancy could be observed.

In the annealing study, two annealing phases of the divacancy were observed that were not reported in electron-irradiated samples – one in the temperature range 350 to 400 K and the other in the temperature range 440 K to 550 K.

In the range 440 K to 550 K, the annealing was visible in both peaks corresponding to the divacancy, providing strong evidence that the defect annealing out, was the divacancy. We propose that this is due to clusters breaking up releasing interstitials.

In the range of 350 K to 400 K, the annealing seems to be in only one of the peaks corresponding to the divacancy. This provides strong evidence that this might be due to a new defect level. The activation energy and apparent capture cross-section for the doubly-charged divacancy was found to be slightly different before and after annealing, again suggesting that there exists a new unknown defect. It was also found that the doubly-charged divacancy are introduced linearly as a function of time under a constant fluence of alpha-particle irradiation. However, it has been shown that the introduction rate of the new unknown defect is dependent on the concentration of the doubly-charged divacancy and increases quadratically with time. Both of these defects are introduced uniformly beneath the surface of the sample. Since there was not a large change in the DLTS signature of the peak, this defect should have a DLTS signature close to that of the $V_2^{(=/-)}$ defect level. This new unknown defect can only be seen in high energy or heavy particle irradiation.

Future work:

Isothermal annealing is needed to determine the annealing activation energy and the frequency factor, in order to determine the mechanism by which annealing occurs. By obtaining the true capture cross-section and a more accurate value for the activation energy, then one would be able to conclusively say that both defects are the same. In other words more electrical properties of the defects at both peaks needs to be done, to fully characterise this new unknown defect. In addition, by careful subtraction of transients, it may be possible to characterise the new defect in isolation.

Bibliography

[1] W.R. Runyan. *Silicon semiconductor technology*. 1st Ed. McGraw-Hill, 1965.

[2] F.D. Auret and P.N.K. Deenapanray. “Deep-level transient spectroscopy of defects in high-energy light-particle irradiated Si.” In: *Critical Reviews in Solid State and Materials Sciences* 29.1 (2010), pp. 1 –44.

[3] Donald A. Neamen. *Semiconductor physics and devices*. 4th Ed. McGraw-Hill, 2012.

[4] S.M. Sze. *Physics of semiconductor devices*. 2nd Ed. Wiley-Interscience, 1936.

[5] C. Kittel. *Introduction to solid state physics*. 7th Ed. John Wiley Sons, 1976.

[6] C. Kittel. *Quantum theory of solids*. 2nd Ed. Wiley and Sons, 1963.

[7] S.M. Sze and K. Kwok. *Physics of semiconductor devices*. 3rd Ed. John Wiley and Sons, 2007.

[8] M. Grundmann. *The physics of semiconductors*. 1st Ed. Springer, 2006.

[9] R.A. Smith. *Semiconductor*. 2nd Ed. Cambridge University Press, 1979.

[10] B.G. Streetman and K. Banerjee. *Solid state electronic devices*. 6th Ed. PHI Learning Private Limited, 2009.

[11] S.S. Li. *Semiconductor physical electronics*. 2nd Ed. New York: Springer-Verlag, 2006.

[12] D. Schroder. *Semiconductor material and device characterisation*. 3rd Ed. New York: Wiley, 2006.

[13] S. Sze and K. Kwong. *Semiconductor devices, physics and technology*. 3rd Ed. New York: Wiley, 2006.

[14] M.S. Tyagi. *Introduction to semiconductor materials and devices*. 1st Ed. John Wiley Sons, 1991.

[15] E.H. Rhoderick and R.H. Williams. *Point defects in semiconductors I: Theoretical aspects*. 2nd Ed. Oxford, 1988.

[16] B.G. Streetman. *Solid state electronic devices*. 1st Ed. Englewood Cliffs (New Jersey): Prentice Hall, 19990.

[17] W.E. Meyer. *Digital DLTS studies on radiation induced defects in Si, GaAs and GaN*. University of Pretoria, 2006.

[18] H.A. Bethe. “Theory of the boundary layer of crystal rectifiers”. In: *Radiation Laboratory, Massachusetts Institute of Technology* 43.12 (1942).

[19] M. Lannoo and J. Bourgoin. *Point defects in semiconductors I: Theoretical aspects*. 1st Ed. Berlin: Springer-Verlag, 1981.

[20] F. de Juan, A. Cortijo, and M. Vozmediano. “Dislocations and torsion in graphene and related systems”. In: *Nuclear Physics B* 828.3 (2010), pp. 625 –637.

[21] D. Williams and C. Carter. *Transmissions electron microscopy*. 1st Ed. New York: Springer, 2009.

[22] D. Kopeliovich. *Imperfections of crystal structure.* 2012. URL: https://www.substech.com/dokuwiki/doku.php?id=imperfections_of_crystal_structure (visited on 09/30/2019).

[23] V.A.J. van Lint et al. *Mechanisms of radiation effects in electronic materials*. 1st Ed. John Wiley Sons, 1980.

[24] M. Huhtinen. "Simulation of non-ionising energy loss and defect formation in silicon". In: *Nuclear Instruments and Methods A* 491.1 (2002), pp. 194 –215.

[25] R. Wunstorf. *Systematische untersuchungen zur strahlenreistenz von silizium-detektoren fur die verwendung in Hochenergiephysik-experimenten*. 1st Ed. University of Hamburg, 1992.

[26] B.R. Gossik. "Disordered regions in semiconductors bombarded by fast neutrons". In: *Journal of Applied Physics* 30.8 (1959), pp. 1214 –1218.

[27] J. Stahl. *Defect characterisation in high-purity silicon after gamma and hadron irradiation*. 1st Ed. University of Hamburg, 2004.

[28] F. Honniger. *Radiation damage in silicon: Defect analysis and detector properties*. University of Hamburg, 2007.

[29] J.A. van Vechten and C.D. Thurmond. "Entropy of ionisation and temperature variation of ionisation levels of defects in semiconductors". In: *Physical Review B* 14.8 (1976), pp. 3539 –3550.

[30] M. Moll. et al. "Comparison of defects produced by fast neutrons and C0-60 gammas in high-resistivity silicon detectors using deep-level transient spectroscopy". In: *Nuclear Instruments and Methods in Physics Research Section A: Accelerators, Spectrometers, Detectors and Associated Equipment* 388 (3 1997), pp. 335–339.

[31] M. Moll. "Silicon particle detectors". In: *IEEE Proceedings 1: Solid-state and Electron Devices* 129.1 (1999).

[32] J. Bourgoin and M. Lannoo. "Point defects in semiconductors". In: *Springer Series in Solid-state Sciences* 35.2 (1983).

[33] B.G. Svensson and J.L. Lindstrom. "Kinetic study of the 830-and-889cm^{-1} infrared bands during annealing of irradiated silicon". In: *Physical Review B* 43.3 (1991), pp. 2292 –2298.

[34] J.W. Corbett. *Electron radiation damage in semiconductors and metals*. 1st Ed. Academic Press, 1966.

[35] J. Frenkel. "On pre-breakdown phenomena in insulators and semiconductors". In: *Phys. Rev.* 54.8 (1938), pp. 647 –648.

[36] S. Makram-Ebeid and M. Lannoo. "Effect of electric field on deep-level transients in GaAs and GaP". In: *Applied Physics Letters* 37.5 (1980), pp. 464 –466.

[37] S. Makram-Ebeid and D. Pons. "Phonon assisted tunnel emission of electrons from deep-levels in GaAs". In: *Journal of Applied Physics* 40.12 (1979), pp. 1161 –1172.

[38] S.D. Ganichev et al. "Distinction between the Poole-Frenkel and tunneling models of electric-field-stimulated carrier emission from deep levels in semiconductors". In: *Physical Review B* 61.15 (2000), pp. 10361 –10365.

[39] A.W. Barnard. "Electrical characterization of alpha-particle irradiation-induced defects in germanium". In: (1976).

[40] D.V. Lang. “Deep-level transient spectroscopy: A new method to characterise traps in semiconductors”. In: *Journal of Applied Physics* 45.7 (1974), pp. 3023 – 3032.

[41] L. Dobaczewski et al. “Laplace transform deep-level transient spectroscopic studies of defects in semiconductors”. In: *Journal of Applied Physics* 76.1 (1994), pp. 194–198.

[42] L.A. Kosyachenko. *Solar Cells - New approaches and reviews*. 1st Ed. IntechOpen, 2015.

[43] Antonio Braga and James Wei. *Deep-level transient spectroscopy with the HF2LI lock-in amplifier.* 2015. URL: https://www.zhinst.com/others/en/blogs/deep-level-transient-spectroscopy-using-hf2li-lock-amplifier (visited on 09/30/2019).

[44] A. A. Istratov. “New correlation procedure for the improvement of resolution of deep level transient spectroscopy of semiconductors”. In: *Journal of Applied Physics* 82.6 (Sept. 1997), pp. 2965–2968.

[45] L. Dobaczewski and P. Kaczor. “Laplace transform deep-level transient spectroscopic studies of defects in semiconductors”. In: *Journal of Applied Physics* 76.1 (1994), pp. 194 –198.

[46] D.V. Lang. *Thermally stimulated relaxation in solids*. 1st Ed. Berlin: Springer-Verlag, 1979.

[47] Y. Zohta and M. Watanabe. “On the determination of the spatial distribution of deep centers in semiconducting thin films from capacitance transient spectroscopy”. In: *Journal of Applied Physics* 53.3 (1982), pp. 1809–1811.

[48] P. Bräunlich. *Thermally stimulated relaxation in solids*. 1st Ed. Berlin: Springer-Verlag, 1979.

[49] Physics Open Lab. *Some alpha and beta spectra.* 2016. URL: https://physicsopenlab.org/2016/11/05/some-alpha-spectra/ (visited on 10/30/2019).

[50] J.F. Ziegler, J. Biersack, and U. Littmark. *The stopping and range of ions in matter*. New York: Pergamon, 1983.

[51] Cloud Nyamhere. *Characterization of process and radiation induced defects in Si and Ge using conventional deep level transient spectroscopy (DLTS) and Laplace-DLTS*. University of Pretoria, 2009.

[52] L. Dobaczewski, A.R. Peaker, and Knud Bonde Nielsen. “Laplace-transform deep-level spectroscopy: The technique and its applications to the study of point defects in semiconductors”. In: *Journal of Applied Physics* 96.9 (Sept. 2004), pp. 4689–4728.

[53] A.W. Barnard. *Electrical characterization of alpha-particle irradiation-induced defects in germanium*. University of Pretoria, 2017.

[54] A. Hallen et al. “Lifetime in proton irradiated silicon”. In: *Physical Review* 79 (8 1996), pp. 3906–3914.

[55] L.W. Song et al. “Bistable interstitial-carbon-substitutional-carbon pair in silicon”. In: *Physical Review B* 42 (9 1990), pp. 5765–5783.

[56] L.W. Song and G.D. Watkins. “EPR identification of the single-acceptor state of interstitial carbon in silicon”. In: *Physical Review B* 42.9 (1990), pp. 5759–5764.

[57] J.W. Corbett et al. “Defects in irradiated silicon. II. Infrared absorption of the Si-A center”. In: *Physical Review* 4 (121 1961), pp. 1015–1022.

[58] G.D. Watkins and J.W. Corbett. “Defects in irradiated silicon. I. Electron spin resonance of the Si-A center”. In: *Physical Review* 121.4 (1961), pp. 1001–1014.

[59] C.E. Barnes and G.A. Samara. “Forward bias induced annealing of the E center in silicon”. In: *Applied Physics Letters* 48 (14 1986), pp. 934–936.

[60] L.C. Kimerling, H.M. De Angelis, and J.W. Diebold. “On the role of defect charge state in the stability of point defects in silicon”. In: *Solid State Communications* 16 (1 1975), pp. 171–174.

[61] G.D. Watkins and J.W. Corbett. “Defects in irradiated silicon: Electron paramagnetic resonance and electron-nuclear double resonance of the Si-E center”. In: *Physical Review* 134.5A (1964), A1359–1377.

[62] J.W. Corbett and G.D. Watkins. “Defects in irradiated silicon: Electron paramagnetic resonance of the divancy”. In: *Physical Review A* 138 (2 1965), pp. 543 –555.

[63] P. Pellegrino et al. “Annealing kinetics of vacancy-related defects in low-dose MeV self-ion-implanted n-type silicon”. In: *Physical Review B* 64 (19 2001), pp. 5211 –5221.

[64] A. Chantre and L.C. Kimerling. “Configurationally multistable defect in silicon”. In: *Applied Physics Letters* 48.15 (1986), pp. 1000–1002.

[65] L.W. Song, B.W. Benson, and G.D. Watkins. “New vacancy-related defects in n-type silicon”. In: *Physical Review B* 33 (2 1986), pp. 1452–1455.

[66] G.D. Watkins and K.L. Brower. “EPR Observation of the isolated interstitial carbon atom in silicon”. In: *Physical Review Letters* 36.22 (1976), pp. 1329–1332.

[67] B.G. Svensson et al. “Generation of vacancy-type point defects in single collision cascades during swift-ion bombardment of silicon”. In: *Physical Review B* 55 (16 1997), pp. 10498 –10507.